

Biophysical Determinants for the Viscosity of Concentrated Monoclonal Antibody Solutions

Published as part of the Molecular Pharmaceutics virtual special issue "Research Frontiers in Industrial Drug Delivery and Formulation Science".

Ilaria Mosca,* Kévin Pounot, Christian Beck, Louise Colin, Olga Matsarskaia,* Christoph Grapentin, Tilo Seydel,* and Frank Schreiber*



Cite This: *Mol. Pharmaceutics* 2023, 20, 4698–4713



Read Online

ACCESS |

Metrics & More

Article Recommendations

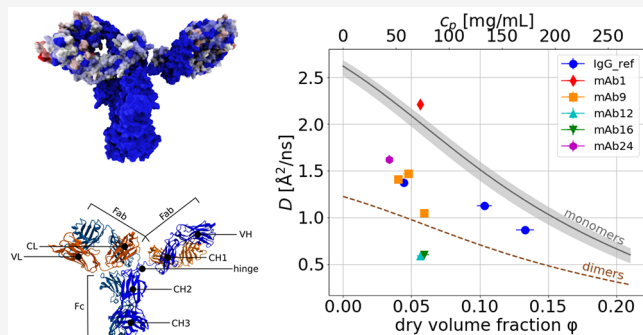
Supporting Information

ABSTRACT: Monoclonal antibodies (mAbs) are particularly relevant for therapeutics due to their high specificity and versatility, and mAb-based drugs are hence used to treat numerous diseases. The increased patient compliance of self-administration motivates the formulation of products for subcutaneous (SC) administration. The associated challenge is to formulate highly concentrated antibody solutions to achieve a significant therapeutic effect, while limiting their viscosity and preserving their physicochemical stability. Protein–protein interactions (PPIs) are in fact the root cause of several potential problems concerning the stability, manufacturability, and delivery of a drug product. The understanding of macroscopic viscosity requires an in-depth knowledge on protein diffusion, PPIs, and self-association/aggregation. Here, we study the self-diffusion of different mAbs of the IgG1 subtype in aqueous solution as a function of the concentration and temperature by quasi-elastic neutron scattering (QENS). QENS allows us to probe the short-time self-diffusion of the molecules and therefore to determine the hydrodynamic mAb cluster size and to gain information on the internal mAb dynamics. Small-angle neutron scattering (SANS) is jointly employed to probe structural details and to understand the nature and intensity of PPIs. Complementary information is provided by molecular dynamics (MD) simulations and viscometry, thus obtaining a comprehensive picture of mAb diffusion.

KEYWORDS: monoclonal antibodies, self-association, self-diffusion, quasi-elastic neutron scattering, small-angle neutron scattering, MD simulations

1. INTRODUCTION

Since the development of the hybridoma technology by Köhler and Milstein,¹ monoclonal antibodies (mAbs) have made their way to therapeutic applications, from 10 mAbs approved by the U.S. Food and Drug Administration (FDA) in 2001² to 100 mAbs in 2021³ to 153 in 2022 (among which 59 were approved for cancer therapy).⁴ The transition from mouse antibodies to chimeric and eventually to human antibodies² has led to a drastically reduced immune reaction and has driven the recent increase in the number of mAbs in use or under development. The actual and potential clinical applications of mAbs cover a wide range of diseases,⁵ including cancers,⁶ infectious and autoimmune diseases (such as rheumatoid arthritis and Crohn's disease),^{7,8} and multiple sclerosis.⁹ The most employed type of mAb for therapeutic use is immunoglobulin G (IgG), which is a Y-shaped molecule of ≈150 kDa. The four main types of IgGs (IgG1, IgG2, IgG3 and IgG4) show very similar structures and amino acid sequences (90% of identity). They differ in their



relative abundance in the serum, their affinity with different types of antigens and receptors, and their half-life.¹⁰ IgGs consist of four polypeptide chains, two heavy chains of ≈50 kDa each and two light chains of ≈25 kDa each, cross-linked by disulfide bonds. Heavy chains contain a variable domain (VH) and three constant domains (CH1, CH2, and CH3), with a flexible hinge region between CH1 and CH2; light chains contain a variable domain (VL) and a constant domain (CL).^{11,14} The segments CH1, VH, CL, and VL form the “fragment antigen binding” (Fab) region, while the CH2 and CH3 domains form the “fragment crystallizable” (Fc) region (Figure 1).^{12,13}

Received: May 20, 2023

Revised: July 18, 2023

Accepted: July 18, 2023

Published: August 7, 2023



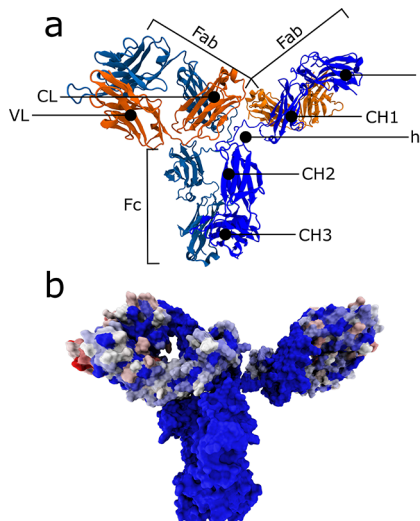


Figure 1. Structure of the mAbs and sequence similarity between the mAbs. (a) The structure of mAb1 was used to represent the mAb using VMD.¹² The different regions of the mAb are annotated on the structure represented using the “NewCartoon” style. The heavy chains are represented in shades of blue, and the light chains are in shades of orange. (b) The sequences of the mAb variants were aligned using the VMD “MultiSeq” module,¹³ and the sequence similarity obtained with the BLOSUM100 matrix is represented with a color range from blue for high similarity to red for low similarity. The different mAbs under study show almost identical structures in the Fc region, while they differ in the extreme parts of the Fab regions (CDR), namely, the ones involved in the binding with the specific antigen.

While polyclonal antibodies are usually produced by several different plasma cell lineages and bind to multiple epitopes, monoclonal antibodies result from the cloning of a unique cell and thus bind only a single epitope.¹⁵ This feature gives mAbs high specificity and high affinity due to the complementarity determining region (CDR) within the Fab, whose shape complements that of the corresponding antigen. The Fc region of mAbs instead allows to reduce side-effects and toxicity compared to polyclonal antibody solutions.⁵ In addition, their half-life can extend to a month after injection thanks to binding to the neonatal Fc receptor. However, their size prevents them from entering cells and crossing the blood-brain barrier. In addition, oral administration results in rapid degradation of the mAbs and limited bioavailability,¹⁶ thus limiting their administration to parenteral routes, namely intravenous (IV), intramuscular (IM) or subcutaneous (SC) injections. Some diseases require life long treatment; IV administration usually demands the stationary treatment of the patient by healthcare professionals, which can compromise patients' flexibility and hence their compliance to therapy. For this reason, mAb delivery via SC injection has recently become a market interest in pharmaceutics, since patients benefit from self-administration with more flexibility, while also ensuring lower healthcare costs.¹⁷

The amount of mAb required to ensure a significant therapeutic effect (typically hundreds of mg) and the typically low injection volume in subcutaneous administration (0.5–2 mL) imply the use of highly concentrated mAb solutions, which can exhibit high viscosities.¹⁸ This potentially affects the stability, manufacturability, and delivery of these biopharmaceuticals.^{19,20} The dynamic viscosity of highly concentrated mAb formulations can easily exceed the tolerance threshold for

injectability ($\sim 15\text{--}20 \text{ mPa}\cdot\text{s}$)²¹ and render their administration difficult or impossible for patients and some injection devices due to the high forces required.^{17,22} Extensive research aiming to minimize the viscosity of highly concentrated mAb solutions is ongoing,¹⁸ along with several studies on the optimization of physicochemical solution stability and manufacturability.^{23,24}

The presence of reversible self-association was proposed as the main mechanism determining viscosity changes in the works by Kanai et al.²⁵ and Liu et al.²⁶ Self-association and hence viscosity of highly concentrated mAb solutions can be influenced by multiple parameters, including concentration, pH, ionic strength,²⁶ or specific interactions, like charge–dipole or dipole–dipole, between domains of monomers.^{27,28} Charged molecules such as NaCl or Arginine-HCl can shield protein charges, thus reducing protein–protein interactions (PPIs) and thereby viscosity.²⁹ Although electrostatic interactions seem to dominate in driving reversible self-association, hydrophobic interactions also play a key role³⁰ and therefore have impact on the solution viscosity. Arginine can also shield antibody hydrophobic interactions,³¹ enhancing its viscosity-reducing function. Other excipients with analogous effects are caffeine,³² hydrophobic salts,³³ or amino acid derivatives,³⁴ but they are not yet employed in commercialized drug products. Addition of viscosity-reducing pharmaceutical excipients to mAb formulations is indeed a common practice and also the subject of continuous research.^{35–37}

More recent work involving experiments and coarse-grained simulations paved the way to viscosity predictors based on amino acid sequence and structural properties of the Fv region.^{38,39} Apgar and co-workers applied the same approach optimizing the charge distribution and hydrophobicity in the variable region (VH and VL) to successfully reduce the viscosity of a mAb solution while preserving its stability and its affinity for the antigen.⁴⁰

Schmitt et al. recently presented a predictive modeling approach for viscosity employing artificial neural networks and based on both experimental and simulation-derived parameters and viscosity data from 27 highly concentrated mAbs,⁴¹ showing that sequence-based optimization of mAb properties is a powerful method for rational mAb design. In addition, recent studies have successfully investigated the link between viscosity and cluster formation using small-angle X-ray scattering (SAXS), micro rheology, and coarse-grained simulations and used cluster theory to predict structure factors of highly concentrated mAb solutions.^{42,43} The same systems have also been investigated using again SAXS, viscometry, and static and dynamic light scattering, in combination with other analytical techniques,⁴⁴ and coarse-grained modeling.⁴⁵ In general, computational approaches, such as coarse-grained and atomistic modeling, hydrodynamic calculations and machine-learning based methods, seem to successfully predict viscosity, intermolecular interactions, aggregation, and physical instabilities in highly concentrated mAb solutions.^{46–50}

Polyclonal antibody solutions have also been widely investigated with SAXS,⁵¹ photocorrelation spectroscopy (XPCS),⁵² quasielastic neutron spectroscopy (QENS) and neutron spin-echo (NSE),⁵³ establishing a quite robust framework for the research on monoclonal antibody solutions. In this area, neutron scattering techniques have already been successfully used⁵⁴ to fully understand the link between macroscopic and microscopic phenomena. For example, neutron reflectometry has been widely employed to study adsorption of mAbs on hydrophobic surfaces, which typically

leads to protein aggregation and degradation.^{55,56} Neutron spin-echo and small-angle neutron scattering (SANS) experiments have identified the formation of dynamic clusters of proteins (including antibodies) in concentrated solutions.^{57,58}

In this context, the self-association or cluster formation of mAbs in aqueous solution can be reliably obtained via the self-diffusion of these clusters measured by high-resolution quasi-elastic neutron spectroscopy (QENS) probing the spatially incoherent scattering and, thus, ensemble-averaged single-particle self-correlation of the mAb hydrogen ¹H atoms. This self-diffusion unambiguously informs the hydrodynamic size of the clusters via the Stokes–Einstein relation. In concentrated solutions of protonated (¹H) proteins in D₂O (²H), the signal from the proteins dominates over the solvent signal in the neutron scattering experiment.

Here, we comprehensively study a set of five different mAbs in terms of this cluster size, which is accessed via their self-diffusion at different temperatures and concentrations in solution, the associated macroscopic viscosity of these solutions, and, for selected samples, their solution structure and PPIs by small-angle neutron scattering (SANS). Moreover, we perform fully atomistic molecular dynamics (MD) simulations to identify possible determinants for the experimentally observed behavior in the sequence of the mAbs. Simultaneously, we also obtained information about the internal diffusive dynamics of these mAbs on the level of protein backbone and side-chain fluctuations from both simulations and QENS spectra. Thus, we associate the macroscopic properties with several microscopic properties in the pursuit of enhancing the understanding required for rational design of high-concentration, low-viscosity mAb formulations. Resulting from the energy resolution of the QENS experiment, diffusion of the proteins is observed during the coherence time of a few nanoseconds. On this time scale, protein–protein collisions can be neglected, and the observed center-of-mass diffusion corresponds to the so-called short-time diffusion, which is governed by hydrodynamic and electrostatic interactions.⁵⁹

2. MATERIALS AND METHODS

2.1. Sample Preparation. We employed five different monoclonal antibodies of IgG1 isotype with κ and λ light chains, with molecular weights (MW) ranging from approximately 145 to 148 kDa and different isoelectric points (pI) ranging from 7.54 to 8.96 (Table S1). In this work, we denote these antibodies as mAb1, mAb9, mAb12, mAb16, and mAb24, consistent with previous work on the same molecules.⁴¹ All mAbs were manufactured in-house at Lonza AG/Ltd. Double gene vectors containing the heavy and light chains were transfected into CHOK1SV GS-KO cells⁶⁰ from Lonza Biologics (Slough, UK) and cultured under selection conditions as stable pooled cultures. Clarified supernatant was obtained by centrifugation followed by filter sterilization using 0.22 μ m filters (Stericup Quick Release from Merck/MilliporeSigma (Darmstadt, DE)), and Protein A chromatography was used for mAb purification. SE-HPLC (size-exclusion high-performance liquid chromatography) showed that all mAbs were >96% monomers, with small amounts of aggregates and fragments. All proteins were concentrated to final concentration of 10 mg/mL (nominal) and buffer-exchanged into the formulation buffer by tangential flow filtration. A 20 mM histidine-HCl (His-HCl) buffer at pH 6.0 was employed as for most (>80%) formulations of highly concentrated approved mAb drug products.⁶¹ All mAb solutions

were then frozen in aliquots, stored at -80 °C, and slowly thawed prior to use.

For QENS and SANS samples, molecules were buffer-exchanged into 20 mM histidine in pure D₂O at pH 6.0, using 3 mL dialysis cassettes containing cellulose membranes with a 30 kDa nominal molecular weight cutoff from ThermoFisher Scientific (Waltham, MA). Two baths of at least 2 h were performed to obtain a dilution factor of at least 10⁴ of residual H₂O in the samples. We remark that exchanging the buffer from H₂O to D₂O is an essential step in neutron experimental techniques because it enables to measure proteins in their aqueous environment while minimizing the scattering signal from the surrounding solvent. Subsequently, the samples were concentrated using 15 mL of 30 kDa Amicon-Ultra concentrators from Merck/MilliporeSigma until the volume needed for the QENS experiment (~800 μ L) was reached. The final concentrations of the samples were determined via UV–vis spectroscopy on dilution series of each mAb using a Jasco V-630 Spectrophotometer. For each dilution step, absorbance curves were collected and their peak values at 280 nm were plotted against the sample reciprocal dilution factor. The data obtained were therefore fitted using the Lambert–Beer law, which links the absorbance A of the sample to its concentration c via $A = \epsilon cl$, with l being the optical path-length, i.e., the thickness of the cuvette, and ϵ being the sample extinction coefficient. The determined concentrations were (76.53 ± 2.59) mg/mL for mAb1, (54.44 ± 1.82), (64.34 ± 4.60), and (80.12 ± 3.65) mg/mL for mAb9, (76.12 ± 3.15) mg/mL for mAb12, (80.44 ± 4.79) mg/mL for mAb16, and (45.38 ± 1.52) mg/mL for mAb24.

For reference, samples of polyclonal IgG solutions were prepared employing lyophilized powder of γ -globulin from bovine serum (≥95% purity, essentially salt-free), purchased from Merck/MilliporeSigma (Darmstadt, DE), and directly dissolved in a 20 mM His-HCl D₂O buffer at pH 6.0. The desired concentrations for these samples were reached and verified via UV–vis using a Nanodrop One Spectrophotometer from ThermoScientific, obtaining three samples at c_p = 60, 140, and 180 mg/mL, respectively.

2.2. Quasi-Elastic Neutron Backscattering Spectroscopy. Quasi-elastic neutron scattering (QENS) accesses molecular dynamics on time and length scales commensurate with the motions of individual proteins and their domains and side chains.

The experiments were performed at the IN16B spectrometer at the Institut Max von Laue - Paul Langevin (ILL, Grenoble, France). This instrument provides an energy resolution of 0.8 μ eV and an energy transfer range of ±30 μ eV, allowing the investigation of motions on a time scale of approximately 100 ps to 10 ns.⁶² IN16B was used with Si(111) monochromator and analyzer crystals, corresponding to an elastic wavelength of 6.27 Å. A linear Doppler motor carrying the monochromator was used to define the energy transfer. The samples were put into double-walled cylindrical aluminum cans with a 0.15 mm gap and an outer diameter of 23 mm, sealed with indium wire, and mounted in a standard cryofurnace for temperature control during the data acquisition. The QENS signal was integrated for 4 h for each sample at each temperature. The QENS data are curated under the DOI 10.5291/ILL-DATA.8-04-908.⁶³ The data were processed with Mantid⁶⁴ applying standard reduction including monitor normalization and empty can subtraction, and subsequently fitted using python employing *scipy.optimize.curve_fit*.⁶⁵

The observable in neutron spectroscopy is the dynamic structure factor $S(q, \omega)$ depending on the energy transfer $\hbar\omega$ and momentum transfer $\hbar q$. IN16B spans a q -range from 0.2 to 1.9 \AA^{-1} , corresponding to lengths from 3 to 30 \AA . S is the sum of the scattering contributions from the aqueous (D_2O) solution and the antibodies. The latter consists of contributions from the global and internal diffusion of the proteins. The superposition of these contributions is convoluted with the spectrometer resolution function $R(q, \omega)$ obtained from a Vanadium calibration measurement. The experimental data were fitted by⁶⁶

$$\begin{aligned} S(q, \omega) = & R(q, \omega) \otimes \{\beta(q)[A_0(q) \mathcal{L}(\gamma(q), \omega) \\ & + (1 - A_0(q)) \mathcal{L}(\gamma(q) + \Gamma(q), \omega)] \\ & + \beta_{\text{D}_2\text{O}}(q) \mathcal{L}(\gamma_{\text{D}_2\text{O}}(q), \omega)\} \end{aligned} \quad (1)$$

where $R(q, \omega)$ is the resolution function $\beta(q)$ and $A_0(q)$ are q -dependent scalars, where the latter is identified with the elastic incoherent structure factor (EISF). The parameters $\beta_{\text{D}_2\text{O}}(q)$ and $\gamma_{\text{D}_2\text{O}}(q)$ were fixed based on measurements of the pure solvent, accounting for the solvent volume excluded by the proteins in $\beta_{\text{D}_2\text{O}}(q)$. Each contribution to $S(q, \omega)$ accounts for a diffusive motion and, thus, is a Lorentzian function $\mathcal{L}(\Gamma, \omega) = \Gamma/\pi(\omega^2 + \Gamma^2)$, whose width provides the associated relaxation rate. $\mathcal{L}(\gamma(q), \omega)$ is the Lorentzian connected to the self-diffusion of the protein center of mass, $\mathcal{L}(\gamma(q) + \Gamma(q), \omega)$ describes the internal diffusive motions, and $\mathcal{L}(\gamma_{\text{D}_2\text{O}}(q), \omega)$ is the signal from the deuterated buffer solution. Samples at $c_p \leq 50 \text{ mg/mL}$ were fitted accounting for just two Lorentzian functions (center of mass and solvent diffusion), due to their lower signal potentially causing overfitting if using eq 1. All samples were prepared in D_2O solutions to reduce the signal from the solvent relative to the protein signal due to the large difference of the incoherent neutron scattering cross sections of hydrogen ${}^1\text{H}$ and deuterium ${}^2\text{H}$.

A two-step approach was used for fitting. First, by q -wise fits, scalar fit parameters were fitted independently for each q . From this procedure we observe that the center-of-mass dynamics follows a Fickian-type diffusion as expected and found previously,⁶⁶ meaning that the width γ of the center of mass Lorentzian is

$$\gamma(q) = Dq^2 \quad (2)$$

where D is the apparent global diffusion coefficient. From a physical point of view, this means that the center of mass exhibits continuous diffusion.

Second, global fits were performed by imposing the q -dependence of some parameters to render the fit more robust and include knowledge on the systems from the q -wise fits, as established in previous works.^{66–69} One approach was to impose a Fickian center of mass diffusion (eq 2) without imposing any q -dependence of the internal diffusion. A q -dependence on the initial guess for the internal dynamics parameters was, however, included, by following the so-called jump-diffusion model⁷⁰

$$\Gamma(q) = \frac{D_{\text{int}}q^2}{1 + D_{\text{int}}\tau q^2} \quad (3)$$

where D_{int} and τ respectively represent the diffusion coefficient related to the internal dynamics and the average residence time in the state of oscillatory motions. A prior knowledge from the q -wise fit was also exploited in the EISF $A_0(q)$, which was parametrized in the global fits as^{67,71,72}

$$A_0(q) = p_0 + (1 - p_0)[p_1 A_{\text{3jump}}(q) + (1 - p_1) A_{\text{sphere}}(q)] \quad (4)$$

i.e., by a superposition of a component accounting for orientational jumps among three sites equally distributed on a circle and placed at distance a one from another.

$$A_{\text{3jump}}(q) = \frac{1}{3[1 + 2j_0(qa)]} \quad (5)$$

and a contribution from diffusion confined in a spherical volume with radius R

$$A_{\text{sphere}}(q) = \left| \frac{3j_1(qR)}{qR} \right|^2 \quad (6)$$

where $j_0 = \sin(x)/x$ and $j_1(x) = \sin(x)/x^2 - \cos(x)/x$ denote the spherical Bessel functions of the zeroth- and first-order, respectively. p_0 (eq 4) is the fraction of hydrogen atoms that appear immobile on the time scale explored by the instrument (elastic contribution), while $(1 - p_0)$ is the fraction of mobile H atoms. In this picture, the coefficients p_1 and $(1 - p_1)$ respectively represent the fraction of H atoms undergoing jump-diffusion among three sites and diffusion confined in a sphere. The first class of H atoms accounts for methyl groups, the reorientations of which are described in eq 5 with the fixed jump distance $a = 1.715 \text{ \AA}$. In this interpretation, H atoms jump between three sites at an angular distance of 120° . The second class of H atoms, namely, those undergoing diffusion inside a sphere (eq 6), accounts for the protein backbone, with R being a free fit parameter. The q -dependent scalar $\beta(q)$ in eq 1 accounts for the thermal Debye–Waller factor due to vibrational motions of hydrogen atoms:

$$\beta(q) \propto \exp\left(-\frac{1}{3}\langle r^2 \rangle q^2\right) \quad (7)$$

with $\langle r^2 \rangle$ being the corresponding mean square displacement (MSD).

2.3. Small-Angle Neutron Scattering (SANS). Small-angle neutron scattering (SANS) was performed on a subset of the antibodies, namely, mAb9, mAb12, and mAb24, in order to determine their time-averaged structural and thermodynamical properties as a function of temperature and protein type. The SANS experiments were carried out on D11⁷³ at the ILL. mAb samples at 80 mg/mL each were filled into 1 mm round quartz cuvettes (Hellma, Mülheim, Germany) and placed onto a copper sample holder. A q range of 0.006 – 0.7 \AA^{-1} was covered by two sample-to-detector distances (16 and 1.7 m) with respective collimation lengths of 16.5 and 2.5 m. A wavelength of 4.6 \AA with a full width-half-maximum (fwhm) wavelength spread of 9% was used. Scattered neutrons were detected using a multitube ${}^3\text{He}$ gas detector with a pixel size of $4 \times 8 \text{ mm}^2$. Raw data were saved in the .nxs (NeXuS) format.^{74,75} Data reduction was performed using Mantid.⁶⁴ All data were corrected for empty cell scattering, transmission (by measurements performed using beam attenuators), and electronic noise (by measuring a ${}^{10}\text{B}_4\text{C}$ absorber). Calibration to absolute scale was

performed using attenuated direct beam measurements. Scattering of the solvent (20 mM His-HCl deuterated buffer at pH 6.0) was subtracted from sample scattering. The SANS data are curated under DOI: 10.5291/ILL-DATA.8-04-923.⁷⁶

2.4. Viscometry. All mAb samples were characterized by viscometry as reported in Schmitt et al.⁴¹ They were measured at $T = 25^\circ\text{C}$ ($\sim 298 \text{ K}$) in their original 20 mM His-HCl aqueous buffer at pH 6.0. In addition, a subset of the antibodies (mAb9, mAb12, mAb16 and polyclonal IgG) was measured in the corresponding deuterated buffer at the same nominal concentrations at 7, 22, and 37°C (280, 295, and 310 K), to collect complementary information on viscosity for the conditions studied in neutron experiments. The procedure used for preparation is the same as the one described for QENS and SANS samples in section 2.1, with dilutions from 180 to 30 mg/mL.

The employed apparatus was a Rheosense VROC Initium rheometer (San Ramon, CA) equipped with a B05 chip and operating using VROC (Viscometer/Rheometer-on-a-Chip) technology⁷⁷ (<https://www.rheosense.com/technology>). A medical-grade viscosity standard from Paragon Scientific (ISO 17025 and 17034), reporting a dynamic viscosity of 9.994 mPas and a density of 1.1567 g/mL at 25°C , was used for the system suitability test (SST). The protocol consisted in measuring the dynamic viscosity of each sample ten times at 25°C while applying an automatic shear rate, which is determined by the instrument software in order to induce a pressure inside the chip targeting the 50% of the full instrumental range.⁴¹

2.5. Sample Characterization by DLS, SLS, and HIC. Dynamic light scattering (DLS), static light scattering (SLS), and hydrophobic interaction column (HIC) measurements were carried out by Schmitt et al.,⁴¹ and these data were used as input for the simulations.

2.6. MD Simulations. **2.6.1. Single-Molecule Simulations and Analysis.** The Protein Data Bank (PDB) files for the different mAbs available internally at Lonza were employed to run single-molecule simulations using NAMD⁷⁸ with the CHARMM36 force field.^{79,80} For each antibody, the starting condition was to place a single monomer in a box with explicit water (TIP3 model)⁸¹ using the solvate plugin of VMD¹² with a padding distance of 25 Å. The system was neutralized (every charge having a counter-charge) using Na^+ and Cl^- ions to avoid electrostatic artifacts during the simulation using the autoionize plugin of VMD.¹² The pressure was maintained at 1 atm using the Nosé–Hoover Langevin piston algorithm,^{82,83} and the temperature was controlled using Langevin dynamics. All bonds were constrained with the SHAKE algorithm.⁸³ The integration of the equation of motions was performed using the Verlet-I/r-RESPA algorithm^{84,85} with integration time of 2, 2, and 4 fs for the short-range bonded and nonbonded forces and long-range forces, respectively. The electrostatic interactions were computed using the Ewald summation method^{86,87} with a smooth switching function between 12 and 14 Å. The five systems, mAb1, mAb9, mAb12, mAb16 and mAb24, were equilibrated at 300 K in the *NVT* (N = number of atoms, V = volume, T = temperature) ensemble for 2 ns to remove any bad contacts that may occur during model building. The *NPT* (P = pressure) ensemble was then used for 60 ns of equilibration at 300 K. The production runs were performed for 120 ns in the *NVT* ensemble to match the experimental conditions where V and T are fixed.

The features (mean-square displacement (MSD), angles between the lobes) were computed using the block average

method.⁸⁸ Briefly, the simulation trajectory is divided into blocks of an increasing size. For each block at a given size, the observable area and its standard deviation between the blocks are computed. The standard deviation is expected to reach a plateau value when the sampling is sufficient for the computed observable⁸⁸ (Figure S7). The minimum block size is defined when the standard deviation reaches the plateau, and that block size is used for calculating the variable average and standard deviation. Using this block average method, the large scale motions of the lobes are computed by taking the scalar product of the normalized position vectors to extract the angles. Subsequently, for different time origins, the deviation of the angle from the initial value is computed. The result is averaged over the blocks, and the standard deviation between the blocks is extracted. The mean-square displacement (MSD) is obtained as

$$\text{MSD} = \langle u^2 \rangle = \frac{1}{N} \sum_i^N \langle \|\vec{r}_i(t_0 + \Delta t) - \vec{r}_i(t_0)\|^2 \rangle \quad (8)$$

where $\vec{r}_i(t)$ is the position vector of atom i at time t and the angular brackets denote the average over multiple time origins.

2.6.2. Feature Extraction from the Structure and the Sequence. To obtain the charge at pH 6, a protein structure file in the .pqr format was generated using *pdb2pqr*⁸⁹ along with *propKa*⁹⁰ to assign the expected protonation states. The charges of the different protein domains are then extracted by summing the charges of the atoms pertaining to a given domain. The other features, namely isoelectric point (pI), grand average of hydropathy (GRAVY) index, and aromaticity were obtained using the BioPython⁹¹ package.

2.6.3. Simulations at High Concentration, Computed SANS Profiles. The system was constructed by randomly placing 6 monomers into a simulation box using the VMD¹² tcl script. The preparation of the system and the simulations were performed using a modified GROMACS^{92,93} package (GROMACS-SWAXS)⁹⁴ designed for interfacing with experimental small-angle scattering data. As above, the CHARMM36 force field was used, the proteins were solvated using TIP3P water, and the system was neutralized with NaCl using GROMACS command-line tools. The 10 ns equilibration and 200 ns simulation runs were performed using the same algorithms cited above. The computed SANS curves were obtained by averaging 100 frames on the last 20 ns of simulation for mAb9, mAb12, and mAb24. An envelope of 0.7 nm from the protein surface was used. Further analysis of protein contacts network and hydrogen bonds was conducted using the MDAnalysis package.^{95,96} Protein network graphs were generated by finding the minimum distance between the pairs of monomers for each frame in the simulation. Subsequently, all pairs for which the minimum distance was lower than or equal to 5 Å were registered as interacting for the frame concerned. Among these interacting pairs, only the ones whose interactions were lasting for more than 1 ns were kept and used to produce the protein network graphs (Figure 10). The number of times a given pair is involved in an interaction throughout the simulation was used as a weighing factor to draw the graphs, where a higher number of times is represented by a thicker black line. Graphs were generated and clustering coefficients obtained using the NetworkX Python package.⁹⁷

3. RESULTS AND DISCUSSION

3.1. Viscometry. The viscosity was analyzed depending on antibody concentration c_p and volume fraction φ (Figure 2). φ is

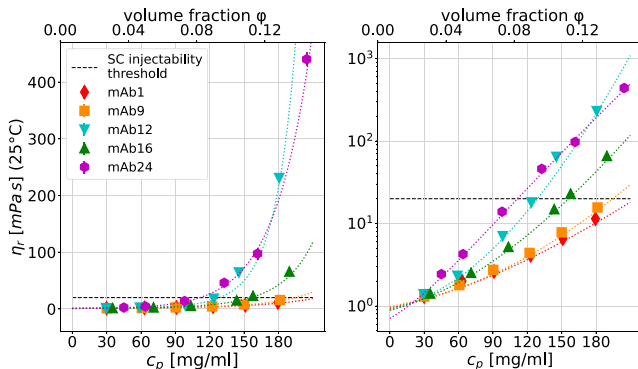


Figure 2. Linear (left) and logarithmic (right) plots showing the relative viscosity $\eta_r = \eta / \eta_0$ (symbols) of aqueous (H_2O) solutions of different mAbs of the IgG1 subtype produced and characterized at Lonza, in 20 mM His-HCl buffer at pH 6.0, at $T = 25\text{ }^\circ\text{C}$ ($\approx 298\text{ K}$), versus mAb concentration c_p (lower x -axis) and volume fraction φ (upper x -axis), from dynamic viscosity measurements using a Rheosense VROC Initium rheometer. Dotted lines are fits to the data using eq 9. The black dashed line represents the typically defined viscosity threshold for syringeability ($\sim 15\text{--}20\text{ mPa}\cdot\text{s}$ used in this work as guidance value, but in practical terms depending on volume, syringe, needle, and acceptable injection force). The strong dependence of the viscosity on the mAbs, in spite of them only differing in the CDR (Figure 1), underlines the need for understanding its microscopic origins.

calculated from the protein concentration c_p as $\varphi = c_p / \nu_s$, assuming the specific volume $\nu_s = 0.739\text{ mL/g}$.⁶⁷ An increase in the viscosity of the solutions at increasing antibody concentrations is observed. This increase follows an exponential trend and shows large differences among the mAbs. In addition, some of them already exceed 15–20 mPa·s at relatively low protein concentration. Data obtained were fitted using the heuristic model

$$\eta_r(\varphi) = \frac{\eta}{\eta_0} = 1 + \exp(a\varphi + b\varphi^2) \quad (9)$$

with η_0 representing the solvent viscosity and a and b being scalar fit parameters. Data collected from the mAbs in their original H_2O buffer are shown in Figure 2; the viscosity of the solvent alone was $\eta_0(H_2O) = 0.92\text{ mPa s}$. Results for the deuterated solutions are reported in the Supporting Information.

The data show a strong dependence of the viscosity η on the type of mAb, although their structures differ only in the Fab and CDR regions. This observation suggests the microscopic origins of this phenomenon and underlines the importance of investigating the interactions between mAb molecules.

3.2. Dynamic and Static Light Scattering. Parameters obtained via light scattering measurements can give indications of the interactions between mAbs in solution. In particular, the second virial coefficient A_2 can be obtained from static light scattering (SLS) and the diffusion-interaction parameter k_D from dynamic light scattering (DLS). In Table 1, we report the values determined previously by Schmitt et al.⁴¹ mAb1 and mAb9 are characterized by larger positive values of A_2 , which are pointing toward electrostatic repulsion and might explain the relatively low viscosity. In contrast to mAb1 and mAb9, mAb12 shows still positive but slightly smaller A_2 , indicating the presence of weaker repulsive forces between its monomers. However, mAb12 undergoes a significant increase in the

Table 1. Second Virial Coefficients A_2 Determined by SLS and Diffusion-Interaction Parameters k_D from DLS Obtained for the Five mAbs by Schmitt et al.⁴¹

mAb	$A_2 \times 10^{-4}$ (mol mL/g^2)	k_D (mg/L)
mAb1	1.96	19.40
mAb9	1.10	18.50
mAb12	0.44	1.37
mAb16	-0.11	-6.17
mAb24	-0.72	-21.10

viscosity at high concentrations compared to mAb1 and mAb9. On the other hand, mAb16 and mAb24 feature negative A_2 values, suggesting the presence of attractive interactions between monomers and justifying their viscosity increase at increasing mAb volume fraction.

Concerning the diffusion-interaction parameter k_D , $k_D > 0$ indicates net repulsive interactions, whereas $k_D < 0$ is a signature of net attractive interactions between mAb monomers.²⁹ Again, while mAb1 and mAb9 show almost equal and largely positive k_D values, mAb12 has a weakly positive k_D , meaning that mAb1 and mAb9 feature much more repulsive PPIs and lower viscosities than mAb12. An opposite behavior is observed for mAb16 and mAb24, which are characterized by negative k_D and therefore experience attractive PPIs and higher viscosities. Moreover, the trend of increasing viscosity at increasing mAb concentration is more pronounced for mAb24, having $A_2 = -0.72\text{ mol mL/g}^2$ and a largely negative k_D (Table 1).

3.3. Quasi-Elastic Neutron Spectroscopy. QENS spectra from different mAb solutions at comparable protein concentration c_p at the same temperature and same momentum transfer q show significant differences (Figure 3) already visible without modeling.

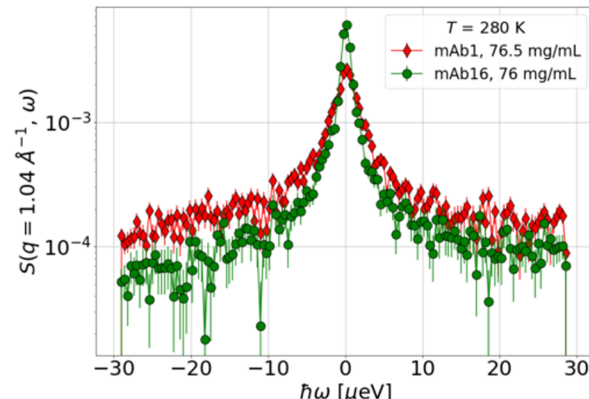


Figure 3. Model-free comparison of QENS spectra at $q = 1.04\text{ \AA}^{-1}$ for $T = 280\text{ K}$ from two mAbs (mAb1 and mAb16) in D_2O solutions with 20 mM His-HCl, at nearly the same protein concentration ($\sim 76\text{ mg/mL}$). Despite the identical conditions, the two spectra show significant differences in intensity and width.

3.3.1. Global Self-Diffusion Varies Substantially among the mAbs. Due to the dominant nuclear incoherent scattering from the proteins, the obtained dynamic structure factor represents the ensemble-averaged single-particle self-dynamics. From the narrowest Lorentzian contribution in the QENS spectra, the observable apparent global self-diffusion coefficients $D = D(D_r, D_t)$ were obtained, which contain the contributions from both rotational D_r and translational D_t diffusion. $D = D(\varphi)$ is sensitive to the crowding effects mediated by hydrodynamic and

electrostatic interactions, but also to the presence of clusters, which can be transient.⁶⁹ The comparison with existing models from colloid theory gives hints on the factors affecting short-time diffusion and, ultimately, viscosity.

3.3.2. Diffusion of Antibody Solutions As Soft Colloid Suspensions. As stated above, proteins in solution experience both translational center-of-mass diffusion and rotational diffusion. The measured dynamic structure factor contains both contributions, which together account for the global dynamics and result in the observable D . The width $\gamma(q)$ of the first Lorentzian contribution in eq 2 is associated with the apparent diffusion coefficient D (Figure 4). To interpret the

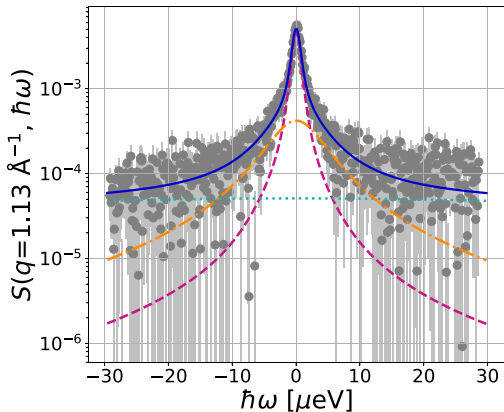


Figure 4. QENS spectrum (symbols) obtained from mAb16 at $c_p = (80.44 \pm 4.79)$ mg/mL at $T = 280$ K with different dynamic contributions (lines) at $q = 1.13 \text{ \AA}^{-1}$. The blue solid line represents the fit consisting of the different dynamical contributions in eq 1: global (magenta dashed line), internal (orange dashed and dotted line), and solvent diffusion (cyan dotted line).

experimental D in terms of colloid physics, a theoretical $D^{\text{theo}}(\varphi_t) = D_r^{\text{theo}}(D_t^{\text{theo}}(\varphi_t), D_t^{\text{theo}}(\varphi_t))$ was calculated as established in ref 66, based on an analytical expression for this implicit function and on the protein hydrogen radial density distribution $\rho(r)$ calculated from their PDB structures (see Supporting Information). An interpretation of the φ -dependence of D in terms of colloid physics is only possible by simplifying the protein shape.^{98–100} Due to the observation time of our backscattering experiment of a few nanoseconds, resulting from its energy resolution, we access the diffusion in the so-called short-time limit, where protein–protein collisions can be neglected and hydrodynamic as well as electrostatic interactions prevail.

In a strongly simplified picture, the mAbs may be approximated as colloidal hard spheres to obtain an analytical expression of the crowding dependence of the translational diffusion D_t^{theo}

$$D_t^{\text{theo}}(\varphi_t) = D_t(\varphi_t = 0)f(\varphi_t) = D_t(0)f(\varphi_t) \quad (10)$$

in which the theoretical reduced translational diffusion $f(\varphi_t)$ depending on the hydrodynamic volume fraction φ_t can be described by a polynomial expression,⁹⁸ and $D_t(0)$ denotes the dilute limit translational diffusion coefficient.⁹⁸ The rotational diffusion can be approximated by the charged-sphere model⁹⁹

$$D_r^{\text{theo}}(\varphi_t) = D_r(\varphi_t = 0)(1 - 1.3\varphi_t^2) \quad (11)$$

where $D_r(0)$ denotes the dilute limit rotational diffusion coefficient,⁹⁹ and which holds for low volume fractions. Due

to the protein hydration shell moving along with the proteins an effective hydrodynamic volume fraction φ_t was assumed.⁶⁶ φ_t is connected to the protein volume fraction φ given by the sample preparation employing a dry protein powder by

$$\varphi_t = \varphi \left(\frac{R_h}{R_{\text{dry}}} \right)^3 \quad (12)$$

such that the volume fraction is rescaled by the ratio between the hydrodynamic radius obtained from the Stokes–Einstein relation

$$R_h = (K_b T) / (6\pi\eta_{\text{D}_2\text{O}}(T) D_t(0)) \quad (13)$$

and the bare effective antibody radius

$$R_{\text{dry}} = \sqrt[3]{3V_{\text{dry}}/4\pi} \quad (14)$$

All parameters entering these calculations, namely, $D_t(0)$, $D_r(0)$, and the bare antibody volume V_{dry} to calculate R_{dry} , were derived via HYDROPRO10¹⁰¹ employing the pdb structure for each mAb, and for the reference polyclonal IgG using the structures of murine and human immunoglobulin G.^{102,14} For consistency with the neutron data, HYDROPRO10 calculations were performed using the viscosity and solution density of D_2O .¹⁰³ Values calculated for 7, 22, and 37 °C (280, 295, and 310 K) can be found in Table S2. Figure 5 depicts the summary (at $T = 280$, 295, and 310 K) comparing the experimental D (symbols) for the different mAbs and an average of $D^{\text{theo}} = D^{\text{theo}}(D_t^{\text{theo}}, D_r^{\text{theo}})$ for monomeric solutions of all mAbs (lines). Gray shaded areas can be uncertainties associated with the solid lines and represent the regions delimited by D^{theo} for the structure of immunoglobulin (PDB ID1IIGT, lower) and mAb12 (upper limit). Dashed brown lines are the approximated dimer curves obtained by rescaling the monomer ones by the dilute limit $D^{\text{theo}}(0)$ of the dimeric immunoglobulin IgA solution structure (PDB ID2QTJ).¹⁰⁴ Note that $D^{\text{theo}}(0)$ was again a function of its translational and rotational components at the dilute limit $D_t(0)$ and $D_r(0)$, calculated via HYDROPRO10.¹⁰¹ Figure 5 shows that D varies significantly among the 5 mAbs and the reference IgG. The trend in D (Figure 5) follows the trend in η (Figure 2). Highly viscous mAb solutions, e.g., mAb12, display a lower D compared to less viscous ones, e.g., mAb1 and mAb9. The interpretation of the observable apparent diffusion of mAb solutions by colloid physics allows to estimate the level of aggregation in these systems. Diffusion coefficients (symbols) similar to the monomer hard-sphere prediction (solid line) suggest an overall monomeric solution, whereas smaller diffusion coefficients corroborate the presence of antibody aggregates that are mainly dimers or constituted by few monomers, since the symbols are not far from the theoretical prediction of dimer diffusion (dashed lines, Figure 5). As stressed earlier, the hard-sphere model constitutes a very simplistic approximation for the nonspherical antibodies, and the assumption on the ratio R_h/R_{dry} enters sensitively by the third power (eq 12).

The global diffusion also varies with temperature, as expected. Diffusion coefficients increase from 280 to 310 K, meaning that attraction between proteins and self-aggregation is not favored at high temperatures, consistently with SANS results (see section 3.4); mAb clusters overall undergo dissociation when exposed from storage to body temperature (~ 7 to 37 °C).

Moreover, by evaluating eq 7, we find that vibrational mean square displacements $\langle u^2 \rangle$ of hydrogen atoms in the mAbs

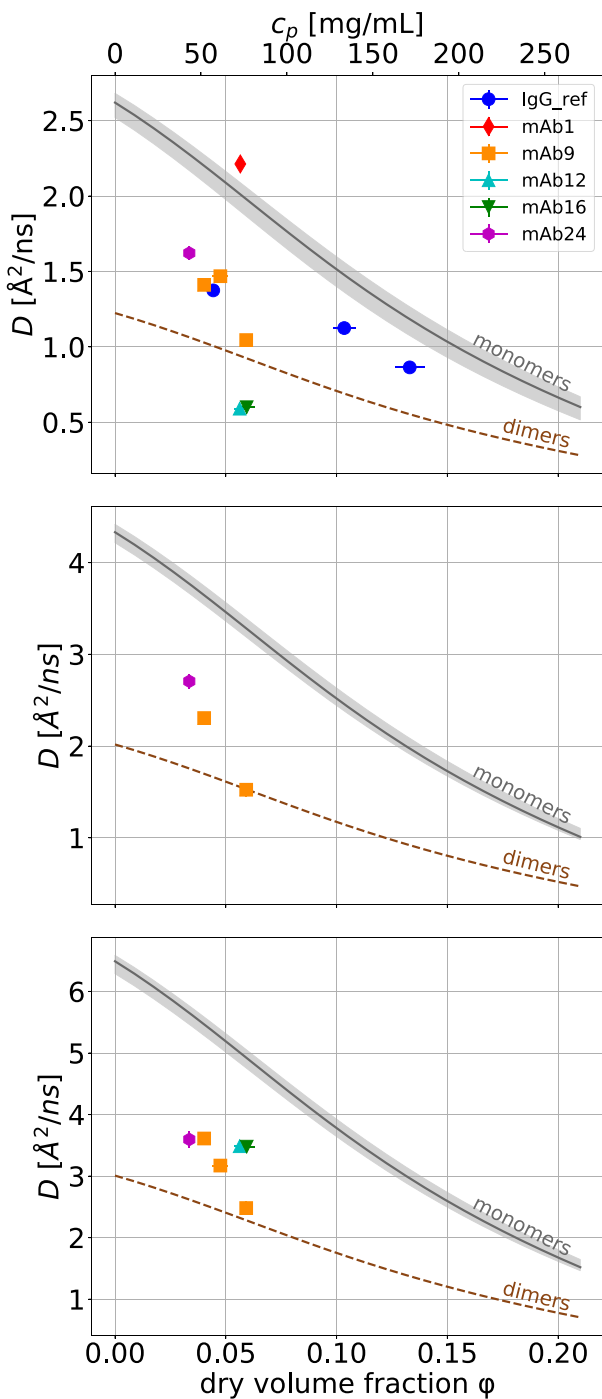


Figure 5. Observable apparent diffusion coefficients D (symbols, obtained from global fits of QENS data) of the mAbs and polyclonal IgG vs protein dry volume fraction ϕ (lower) and concentration c_p (upper x-axis) in solution at $T = 280 \text{ K}$ (top), $T = 295 \text{ K}$ (center), and $T = 310 \text{ K}$ (bottom). Gray solid lines denote the average value of D^{theo} for monomers of all mAbs, murine and human IgG,¹⁰² obtained using a colloid physics hard-sphere model as explained in the main text. Gray shaded areas are delimited by D^{theo} for IIGT (lower) and mAb12 (upper limit). Dashed brown lines are the approximated dimer curves obtained by rescaling the monomer ones by the dilute limit $D^{\text{theo}}(0)$ of the dimeric immunoglobulin structure (PDB ID 2QTJ).¹⁰⁴ Symbols below the monomer lines corroborate the presence of clusters due to their larger hydrodynamic size. However, these clusters are mainly dimers or formed by a few monomers, and they dissociate at increasing temperature (from approximately storage to body temperature).

studied are in the range of $0.2\text{--}1.2 \text{ \AA}^2$ with the expected temperature dependence, consistent with values found for other proteins.⁶⁸

3.3.3. Internal Dynamics and Viscosity Shows Lower Correlation on Short Time Scales. Generally, protein internal dynamics on picoseconds to several nanoseconds time scales can relate to the capacity of the protein to swiftly change conformation and possibly adopt conformers prone to self-association.⁵⁹ Such behavior would be in favor of high viscosities. Hence, the internal dynamics of the mAbs were investigated experimentally through the QENS spectra and computationally through the MD simulations. The diffusion coefficient associated with internal motions D_i , as obtained from QENS fits, is similar within the confidence bounds for each mAb except for mAb9, for which D_i is around 2 times lower. The residence time τ is similar for all mAbs, with values ranging from 10 to 25 ns, except for mAb1 and mAb9, showing slightly higher values. These ensemble-averaged values for internal dynamics obtained from QENS do not present any clear correlation to the viscosity data in section 3.1.

The large scale domain motions, that is, the angle between the main lobes, Fc and Fab regions of the mAbs, were computed as described in section 2, averaging over time blocks of 20 ns (Figure 6). There are no significant differences between the

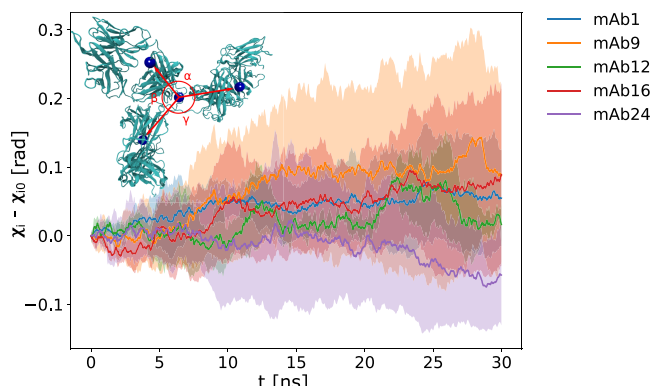


Figure 6. Large-scale domain motions observed during MD simulations of the mAbs. For each angle indicated on the cartoon structure in the inset, the deviation of the angle $\chi_i = \{ \alpha, \beta, \gamma \}$ from the initial value χ_{i0} was computed as indicated in section 2 using the block average method with a block size of 20 ns. The average of the blocks is plotted using colored solid lines and the standard deviation of the blocks using colored shaded areas for each mAb.

different antibodies within the errors, as the angles between the three main lobes of the antibody fluctuate slowly around an equilibrium value. However, the viscosity could depend on weak transient interactions that can be facilitated by fast internal dynamics in the subnanosecond time domain.

To investigate fast motions, the diffusive MSD $\langle u^2 \rangle$ was computed, as explained in section 2 for each amino acid of the different mAbs. The MSD were obtained for a time delay of 50 ps, 200 ps, and 1 ns. Globally, the MSDs appear similar for all mAbs without an obvious correlation with increasing viscosity (Figure 7 (top)). Slightly more relevant differences in the MSD among the mAbs can be found in the light chains (Figure 7, bottom), but without a visually clear trend with increasing viscosity.

To better correlate with the viscosity, the dimension of the MSD vector was reduced by averaging over the main domains (VH, CH1, CH2, CH3, hinge, VL, and CL) for all time delays.

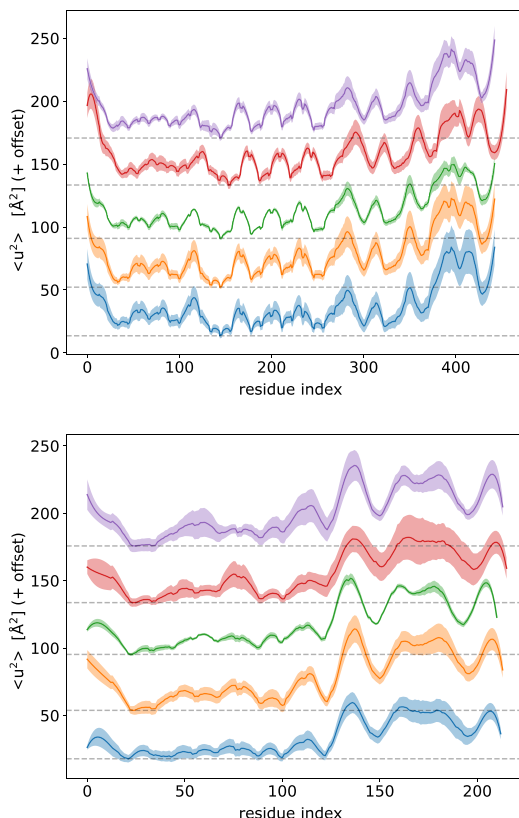


Figure 7. Diffusive mean square displacements (MSD) $\langle u^2 \rangle$ derived from MD simulations of the 5 mAbs computed from the simulated trajectories, as described in section 2. The resulting average over the blocks of 20 ns is plotted for each mAb using solid colored lines and corresponding shaded areas for the standard deviations. MSD for the heavy chains (top) and for the light chains (bottom plot) with an offset on y-axis were used for better visualization and for increasing viscosity from bottom to top.

The resulting correlations with the viscosity are presented in Figure 8. It appears that the viscosity is significantly correlated ($\rho_{\text{viscosity}, \theta_i} > 0.5$) with the features related to PPI strength (virial coefficient A_2 and diffusion-interaction parameter k_D). Moreover, the charge on the VL and VH regions appears to correlate with viscosity as well, suggesting that electrostatic interactions are dominant. The internal dynamics represented by the MSD presents some correlation with viscosity, but the correlation coefficients are systematically lower than 0.5, indicating that such dynamics plays a subordinate role.

To assess whether the features used to compute the correlation can provide a good predictor of viscosities, the viscosity was removed from the data set, resulting in a reduced data set. A principal component analysis (PCA) was performed on the covariance matrix of this reduced data set using routines from the *scikit-learn* package.¹⁰⁵ The observable values from Figure 8 were then projected on the first 3 principal components to visualize how the different mAbs are separated in PCA space (Figure 9). It appears that the use of either the full feature data set or a reduced one where MSD are removed allows for a good separation of the mAbs according to the viscosity. However, the MSDs alone do not provide a good separation of the mAbs and hence do not constitute a reliable predictor for the viscosity.

3.3.4. Viscosity Strongly Depends on VL and VH Domain Charges and Hydrophobicity. To further explore the determinants of the viscosity, additional features, obtained

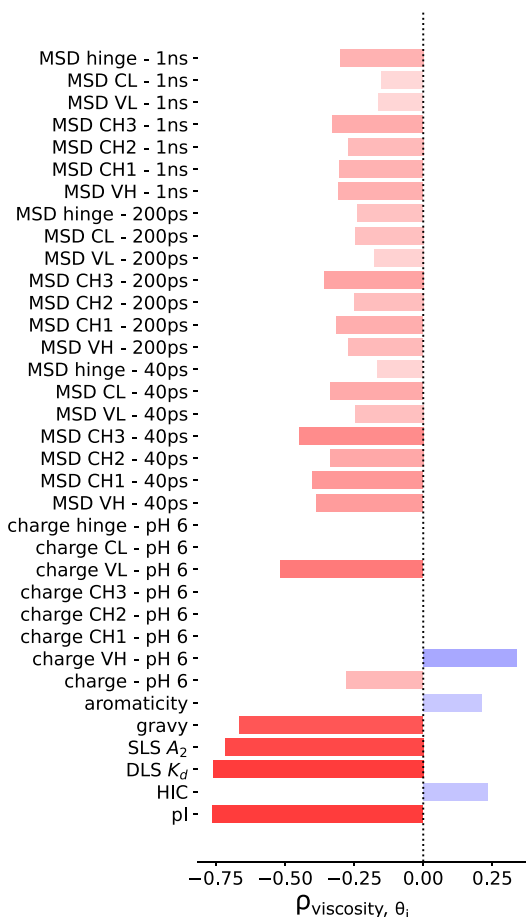


Figure 8. Correlation of viscosity with parameters derived from the protein sequence and MD simulations. The MSD as well as the features extracted from the sequence (see section 2) were used to compute the statistical correlation with the viscosity $\rho_{\text{viscosity}}, \theta_i$ given by $\rho_{x,y} = \frac{\text{covariance}(x,y)}{\sqrt{\sigma(x)} \sqrt{\sigma(y)}}$, where σ is the variance and θ_i is the value of the observable i . The result is shown as a vertical bar plot with the features arranged on the y-axis and the bars ranging from deep red for a correlation of -1 to deep blue for a correlation of 1 . The charges are computed at pH 6 and the labels include the concerned protein domain except for “charge pH 6”, which is the total charge of the protein. The labels for MSD values include the concerned protein domain, followed by the time delay used to compute it.

directly from the amino acid sequence, were computed (see section 2). The obtained features were used to compute the statistical covariance with the viscosity. The input values used for the viscosity were collected from concentration series (30, 60, 90, 120, 150, and 180 mg/mL) of the five mAbs in solution at 25 °C (data in section 3.1). The hydrophobicity and charge, especially on the VL and VH domains, are correlated to the viscosity (Figure 8). The second virial coefficient A_2 , the diffusion-interaction parameter k_D , and the isoelectric point pI present a pronounced correlation with viscosity.

3.3.5. Protein Network Dynamics Differs between mAb9, mAb12, and mAb24. Next, we investigate the PPIs by putting 6 monomers in a simulation box. The simulations were run for 200 ns and analyzed using a protein network graph computation of the hydrogen bond dynamics between individual monomers. Building a protein interaction network allows identification of protein clusters, their size, and their dynamics by tracking the interaction lifetime for each pair of monomers in the simulation.

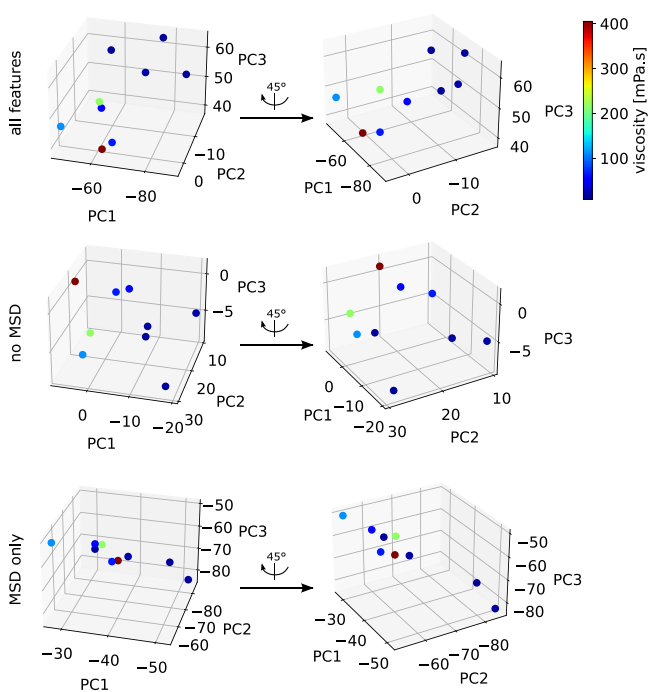


Figure 9. Separation of mAbs using computed features. PCA was performed on the features computed for Figure 8 using routines from the *scikit-learn* Python package.¹⁰⁵ The initial observable vectors were projected on the first 3 principal components (PC) and plotted with dots whose color corresponds to viscosity (ranging from deep blue for low η to brown for high η). Top plots: projections for a PCA using all features; middle plots: projections for a PCA on a data set where the MSD was removed; bottom plots: projections for a PCA performed on a data set containing MSD only.

The network graphs were constructed as described in section 2, and the result is shown in Figure 10. The graph for mAb9 shows two clusters of 4 and 2 monomers that are present for most of the trajectory and can sometimes interact with an interaction lifetime of 1.1 ns, which crosses the backscattering observation time window. The graphs for mAb12 and mAb24 present a higher connectivity quantified by the clustering coefficient (CC) of the graphs, being 0.73 for mAb12 and 0.47 for mAb24, versus a value of 0.36 for mAb9. This result is in agreement with the slow diffusion and the marked trend to cluster of mAb12 revealed by QENS (Figure 5), as well as with its stronger PPIs probed by SANS (Figure 13), compared to the ones present in mAb9 and mAb24 solutions. Moreover, the average relaxation rate (obtained by computing the inverse average lifetime of graph vertices) is lowest for mAb9 and highest for mAb24, thereby demonstrating a more dynamic protein interaction network for mAbs with higher viscosities.

3.4. Small-Angle Neutron Scattering. SANS provides thermodynamic and structural information on the nanometer–micrometer scale. The intensity of scattered neutrons is expressed as^{106,107}

$$I(q) = \frac{d\sigma}{d\Omega}(q) = n(\Delta\rho)^2 V_{part}^2 P(q) S(q) \quad (15)$$

where n is the particle number density, $\Delta\rho$ is the difference in scattering length density between the solvent and the particles (also known as the scattering contrast), and V_{part} is the volume of a single particle.^{106,107} The term $P(q)$ is referred to as the particle form factor, determined by the protein shape.^{108,107} The

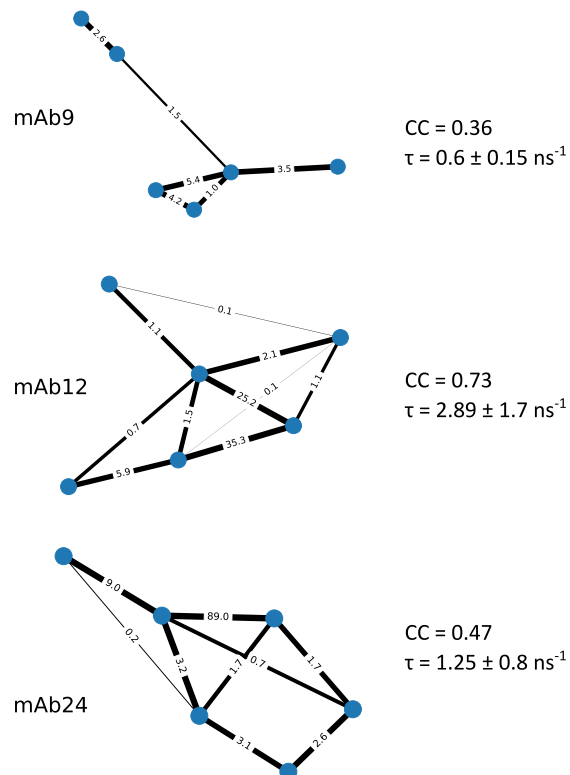


Figure 10. Protein network graphs for mAb9, mAb12, and mAb24, produced from the simulations at high concentration. Each blue node represents a single mAb monomer, and two nodes are connected by an edge when their atoms are at a minimum distance of 5 Å. The width of the edge line is proportional to the number of times a given pair of monomers are in interaction during the simulation, and the number labels indicated on the edges are the average lifetime of the interaction given in nanoseconds. The clustering coefficient (CC) and the average relaxation rate (inverse lifetime) τ are shown for each protein graph. Protein network dynamics at a high concentration strongly depend on the mAb.

structure factor $S(q)$ (details in refs 109–111) characterize the interactions between particles in solution. $S(q \rightarrow 0)$ can be expanded into a series of virial coefficients A_n ^{112–114}

$$S(q \rightarrow 0) = \frac{RT}{M_W} \left(\frac{\partial \Pi}{\partial c} \right)^{-1} = \frac{1}{1 + 2M_W A_2 c + \dots} \quad (16)$$

with M_W (g/mol) as the molecular weight of the particles investigated.

The second virial coefficient B_2 ¹¹⁵

$$B_2 = 2\pi \int_0^\infty dr r^2 [1 - e^{-u(r)/k_B T}] \quad (17)$$

is related to A_2 , which can be determined by SLS (see above)⁴¹ via¹¹⁶

$$B_2 = A_2 \cdot \frac{M_W^2}{N_A} \quad (18)$$

We employ the reduced second virial coefficient B_2^* , defined as the ratio B_2/B_2^{HS} (B_2^{HS} : second virial coefficient for hard spheres) and linked to the stickiness parameter τ by

$$B_2^* = B_2/B_2^{HS} = 1 - \frac{1}{4\tau} \quad (19)$$

where $B_2^{HS} = 2\pi\sigma^3/3$, with σ being the diameter of the hard spheres.¹¹⁵ In the case of the mAb samples studied here, we employ the approach by Da Vela et al.⁵¹ for bovine γ -globulin. The SANS data were fitted using the NIST software package for SANS analysis Igor Pro¹¹⁷ by WaveMetrics, Inc. (Lake Oswego, OR). The model used is a combination of an ellipsoid form factor $P(q)$ (oblate ellipsoid with axes of 7–8 and 58–60 Å) and a sticky hard sphere (SHS) structure factor $S(q)$ for mAb12 and mAb24. For mAb9, the SHS structure factor was not properly fitting the data at low q , so we opted for a simple hard-sphere (HS) potential, also due to the repulsive feature of its $I(q)$ at low q . We note that in spite of the anisotropic shape of mAbs, an isotropic interaction potential is used here. This approach has been justified by Yearley et al.¹¹⁸ and Castellanos et al.¹¹⁹ Background-corrected SANS data for mAb9, mAb12 and mAb24 with the corresponding fits are shown in Figures 11 and 12, in order to better visualize antibody-type and temperature dependence of the data, respectively. Overall, a decrease of the intensity $I(q)$ in the low- q region is observed when the samples are heated up from 21 °C to human-body temperature, suggesting a weaker interprotein attraction at high temperatures and likely dissociation of microscopic aggregates formed at lower temperatures (Figure 11). High- q features of $I(q)$ (around 0.2 Å⁻¹) are due to the molecular shape of the mAbs, which is preserved across the temperature range studied. However, differences in the low- q region are also variant-dependent (Figure 12), meaning that the three mAb solutions feature different PPIs. In fact, mAb9 shows less attractive PPIs than mAb12 and mAb24, which may result in a lower level of clustering and a higher diffusion coefficient, as observed through QENS (Figure 5), along with a lower CC determined from the protein network analysis (Figure 10).

For mAb12 and mAb24, based on the SHS $S(q)$ fit, the normalized second virial coefficient B_2/B_2^{HS} was determined. $B_2/B_2^{HS} < 0$ indicates overall attractive interactions between the mAb molecules, whereas $B_2/B_2^{HS} > 0$ points toward overall repulsive interactions. The resulting B_2/B_2^{HS} values are shown in Figure 13. Lower B_2/B_2^{HS} are observed at lower temperature, which means that mAb–mAb attraction is stronger and aggregation is favored; this result is in agreement with conclusions from QENS data (section 3.3).

For mAb12, the A_2 value mentioned above indicated a slight repulsion, while the B_2/B_2^{HS} values indicate an attraction. This might be due to the usage of the sticky hard sphere model, which is incapable to capture reversible self-association or anisotropic or directional interactions. A reversible self-association would also explain the significantly reduced diffusion coefficient observed above.

4. CONCLUSIONS

The present work provides a deeper understanding of the link between microscopic dynamic properties and macroscopic viscosity of the solutions of five different monoclonal antibodies of the IgG1 subtype. By a multitechnique approach employing neutron backscattering spectroscopy, small-angle neutron scattering, molecular dynamics simulations, and viscometry, we find biophysical determinants for the variation in the viscosity of mAb solutions. Consistent with previous work,^{57,120,121} we identify the formation of clusters of self-associating antibody molecules as the main mechanism responsible for the increase in viscosity at high antibody concentrations.

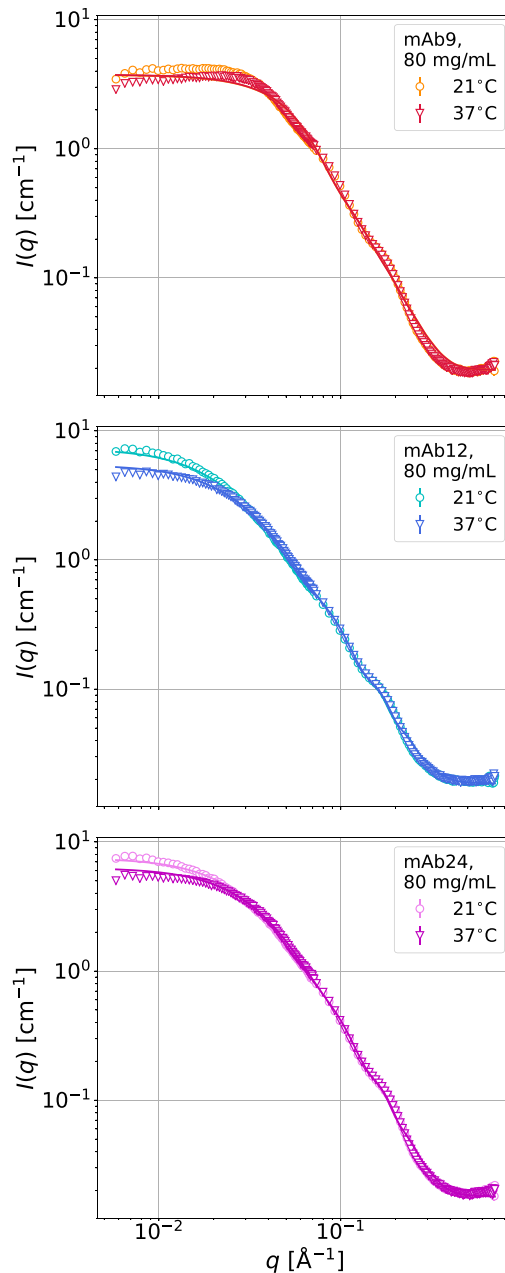


Figure 11. Temperature dependence of mAb–mAb interactions probed using SANS. Experimental curves (empty symbols) and their corresponding fits obtained from a subset of mAbs: mAb9 (top), mAb12 (center), and mAb24 (bottom) at $c_p = 80$ mg/mL in 20 mM His-HCl buffer in D₂O. A decrease in $I(q)$ at low q with increasing temperature T reveals weaker PPIs and a potential dissociation of aggregates.

In particular, QENS experiments provide access to the different dynamical contributions of the systems studied. Global and internal dynamics can be decoupled and analyzed separately. The global dynamics refers to the protein center-of-mass motion, accessing the observable apparent diffusion coefficient D , which can be interpreted in terms of the physics of dense colloidal suspensions of hard spheres, within the approximations of short-time diffusion and an effective spherical shape. By approximating mAb molecules as hard spheres, D obtained from QENS is compared to the theoretical estimation $D_{\text{theo}}(\phi)$ obtained employing the hard-sphere model. Impor-

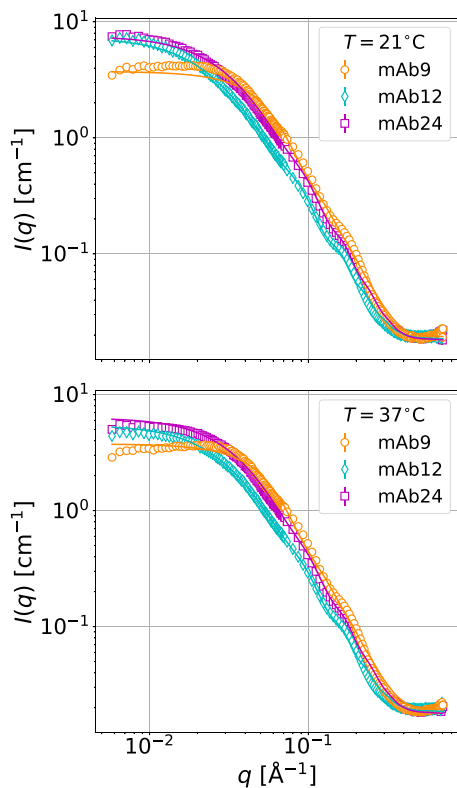


Figure 12. Antibody dependence of PPIs probed through SANS. Comparison among SANS curves (empty symbols) and their corresponding fits of mAb9, mAb12, and mAb24 at 21 °C (left) and 37 °C (right). Protein concentration in all samples is 80 mg/mL in 20 mM His-HCl buffer in D₂O. $I(q)$ does not show significant changes at high- q , while differences in the low- q region are visible at both 21 and 37 °C and suggest the presence of different PPIs in the three mAb solutions. mAb9 shows much less attractive PPIs than mAb12 and mAb24.

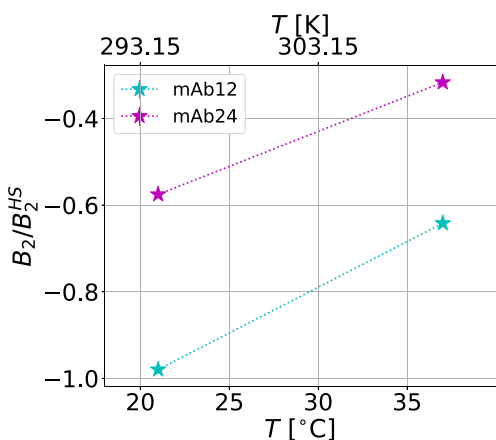


Figure 13. Reduced second virial coefficient B_2/B_2^{HS} (symbols) determined from the SANS fits plotted against temperature T in °C (lower x-axis) and Kelvin (upper x-axis). Data from the two mAbs presented here (mAb12 and mAb24) show an increase in B_2/B_2^{HS} with an increase in temperature from 21 to 37 °C, meaning that attraction among antibodies decreases when the solutions experience higher temperatures. Dashed lines are guides to the eye.

tantly, due to the prevailing nuclear incoherent scattering from the protein hydrogen atoms, our QENS experiment probes the self-diffusion (synonymously: tracer diffusion) of the mAbs. For

this reason it unambiguously provides the hydrodynamic size of the mAb assemblies unobstructed by structural features seen by coherent scattering. For most mAbs, $D < D_{\text{theo}}(\varphi)$ in agreement with a cluster picture. Moreover, most diffusion coefficients are larger than those estimated for mAb dimers, such that the QENS results support a picture of very small clusters with less than two members on average. The clusters may be transient in time, and the QENS spectra are recorded with an observation time of a few nanoseconds resulting from the <1 μeV energy resolution, thus, not ruling out dissociation on longer times. This short observation time comes with the advantage that protein–protein collisions can be neglected, and the observed diffusion is governed by hydrodynamic and electrostatic interactions.

From the QENS analysis we can infer that all mAbs undergo self-association and cluster formation at the lowest temperature measured, 280 K (≈ 7 °C), which is a storage temperature, while short-time diffusion is enhanced at 310 K (≈ 37 °C), which is the physiological temperature. Moreover, different mAbs result in significantly different diffusion with smaller diffusion, i.e., larger average cluster size for higher viscosity.

In addition, all mAbs measured show higher D with increasing temperature, consistent with enhanced diffusion with a higher T as expected. We point out that the mAb concentrations measured by QENS in the present work are low compared to those used in previous studies on model protein solutions.⁵⁹ For this reason, the scattering signal is weak and the accuracy of the information on the internal diffusive dynamics is limited. Nevertheless, this internal dynamics information is consistent with earlier work on γ-globulin⁶⁷ within the uncertainties. The low signal required that global fits of the spectra for all momentum transfers at once had to be used. These global fits might result in a systematic error for the global diffusion due to possible cross-talk of the global and internal dynamics Lorentzians at large momentum transfers.

SANS was used to probe structural and thermodynamic features of mAb solutions on a subset of the mAbs studied by QENS, and the second virial coefficient was extracted to estimate the interaction among mAb molecules, revealing that protein–protein attraction decreases with decreasing viscosity and increasing temperature. This trend is consistent with the cluster formation seen in QENS. Our data set indicates that the clusters tend to dissociate with increasing temperature, the weak electrostatic interactions being outweighed at higher temperatures. As the data set is currently limited, this trend should be substantiated with further measurements in the future.

The single-molecule MD simulations provide an atomistic view of the internal dynamics, complementary to the QENS data. The result shows that the internal dynamics are not a good predictor of the viscosity. The internal dynamics was found to be similar for all mAbs, as expected based on the fact that the molecules are basically identical apart from small differences in the CDR regions of their sequences. The presence of a strong correlation of viscosity with hydrophobicity second virial coefficient and diffusion-interaction parameter indicates that PPIs and possibly protein–solvent interactions mainly drive the viscosity. The MD simulations with 6 molecules per simulation box provide some insight on the protein cluster dynamics for mAb9, mAb12, and mAb24. It appears that high viscosity mAbs tend to form clusters with more monomers but with shorter interaction lifetimes and less frequent pairs of monomers such that the protein network reorganizes faster. As a result of strong cluster dynamics, shear stress results in inefficient momentum transfer between molecules because of short-lived interactions,

high friction between clusters, and hence high viscosity. We note that the conclusions from the simulations are limited by the achievable sampling time. Yet, the results are convincing and appeal for further work fully dedicated to simulations of mAbs at high concentration.

We have presented an extended study of an unprecedentedly large number of different mAbs with neutron and complementary techniques and have established incoherent high-resolution neutron backscattering spectroscopy as a new technique to study mAb solutions and to unambiguously access their average hydrodynamic cluster size. A key finding from this work is that the clusters seen on the nanosecond observation time of our neutron spectroscopy experiment consist on average of less than two members per cluster at physiological temperature (Figure 5, bottom). This average size can be assumed to reflect a highly dynamic picture of the self-association and resulting viscosity of the mAb solutions and depends sensitively on the type of mAb. The sensitivity on the mAb type cannot be understood by internal motion, as revealed by the simulations, but rather by differences in the mAbs in specific regions near the protein surface. The simulations are consistent with this picture of a highly dynamic transient protein association.

■ ASSOCIATED CONTENT

Data Availability Statement

Neutron data are permanently curated under DOI and available at refs 63 and 76.

■ Supporting Information

The Supporting Information is available free of charge at <https://pubs.acs.org/doi/10.1021/acs.molpharmaceut.3c00440>.

Biophysical properties of mAbs, viscometry on deuterated antibody solutions, additional example neutron spectra, HYDROPRO10 calculations and hydrogen density distributions from PDB structures, additional QENS/SANS fit parameters and simulation results ([PDF](#))

■ AUTHOR INFORMATION

Corresponding Authors

Frank Schreiber — Institut für Angewandte Physik, Universität Tübingen, Tübingen 72076, Germany;  orcid.org/0000-0003-3659-6718; Email: frank.schreiber@uni-tuebingen.de

Tilo Seydel — Institut Max von Laue - Paul Langevin, Grenoble 38042, France;  orcid.org/0000-0001-9630-1630; Email: seydel@ill.eu

Olga Matsarskaia — Institut Max von Laue - Paul Langevin, Grenoble 38042, France;  orcid.org/0000-0002-7293-7287; Email: matsarskaia@ill.eu

Ilaria Mosca — Institut für Angewandte Physik, Universität Tübingen, Tübingen 72076, Germany; Institut Max von Laue - Paul Langevin, Grenoble 38042, France;  orcid.org/0001-9211-5697; Email: mosca@ill.eu

Authors

Kévin Pounot — Institut für Angewandte Physik, Universität Tübingen, Tübingen 72076, Germany; Institut Max von Laue - Paul Langevin, Grenoble 38042, France; Present Address: European Synchrotron Radiation Facility, 71 Av. des Martyrs, Grenoble 38042, France

Christian Beck — Institut für Angewandte Physik, Universität Tübingen, Tübingen 72076, Germany; Institut Max von Laue - Paul Langevin, Grenoble 38042, France;  orcid.org/0000-0001-7214-3447

Louise Colin — Institut für Angewandte Physik, Universität Tübingen, Tübingen 72076, Germany; Institut Max von Laue - Paul Langevin, Grenoble 38042, France

Christoph Grapentin — Lonza AG/Ltd., Basel 4057, Switzerland

Complete contact information is available at:

<https://pubs.acs.org/10.1021/acs.molpharmaceut.3c00440>

Author Contributions

All authors performed experiments, contributed to data analysis and in writing the manuscript. K.P. performed simulations, L.C., K.P., and C.B. prepared the samples. F.S., T.S., O.M., and C.G. designed the research and are coproposers and supervisors of the associated InnovaXN project (innovaxn.eu).

Notes

The authors declare no competing financial interest.

■ ACKNOWLEDGMENTS

This research has been supported by InnovaXN, a EU Horizon 2020 MSCA COFUND programme (innovaxn.eu, grant agreement no. 847439). I.M. acknowledges an ILL Ph.D. studentship funded by this programme. Moreover, the authors are grateful for support by the DFG and ANR (ANR-16-CE92-0009, ImmunoglobulinCrowding), notably in the initial phase of this project, and by the BMBF (ErUM-pro 05K19VTB and 05K22VTA). The authors acknowledge the support of the ESRF and ILL for using the platforms of the Partnership for Soft Condensed Matter (PSCM). The authors are also thankful to Trevor Forsyth, Michael Haertlein, and Juliette Devos (ILL, Grenoble) for advice and for providing access to the Life Science lab facilities. We thank Jonathan Schmitt (Lonza Basel) for support with rheometry.

■ REFERENCES

- (1) Köhler, G.; Milstein, C. Continuous Cultures of Fused Cells Secreting Antibody of Predefined Specificity. *Nature* **1975**, *256*, 495–497.
- (2) Lonberg, N. Human Antibodies from Transgenic Animals. *Nat. Biotechnol.* **2005**, *23*, 1117–1125.
- (3) Mullard, A. FDA Approves 100th Monoclonal Antibody Product. *Nat. Rev. Drug Discovery* **2021**, *20*, 491–495.
- (4) Hongrong Cai, H.; Pandit, A. A. Therapeutic Monoclonal Antibodies Approved by FDA in 2022 (Mini Review). *J. Clin. Exp. Immunol.* **2023**, *8*, 533–535.
- (5) Castelli, M. S.; McGonigle, P.; Hornby, P. J. The Pharmacology and Therapeutic Applications of Monoclonal Antibodies. *Pharmacol. Res. Perspect.* **2019**, *7*, No. e00535.
- (6) Scott, A. M.; Allison, J. P.; Wolchok, J. D. Monoclonal Antibodies in Cancer Therapy. *Cancer Immun.* **2012**, *12*, 14.
- (7) Flego, M.; Ascione, A.; Cianfriglia, M.; Vella, S. Clinical Development of Monoclonal Antibody-Based Drugs in HIV and HCV Diseases. *BMC Medicine* **2013**, *11*, 4.
- (8) Bruno, V.; Battaglia, G.; Nicoletti, F. The Advent of Monoclonal Antibodies in the Treatment of Chronic Autoimmune Diseases. *Neurological Sciences* **2011**, *31*, 283–288.
- (9) Voge, N. V.; Alvarez, E. Monoclonal Antibodies in Multiple Sclerosis: Present and Future. *Biomedicines* **2019**, *7*, 20.
- (10) Vidarsson, G.; Dekkers, G.; Rispens, T. IgG Subclasses and Allotypes: from Structure to Effector Functions. *Front. Immunol.* **2014**, *5*, 520.

- (11) Huber, R.; Deisenhofer, J.; Colman, P. M.; Matsushima, M.; Palm, W. Crystallographic Structure Studies of an IgG Molecule and an Fc Fragment. *Nature* **1976**, *264*, 415–420.
- (12) Humphrey, W.; Dalke, A.; Schulten, K. VMD: Visual Molecular Dynamics. *J. Mol. Graphics* **1996**, *14*, 33–38.
- (13) Eargle, J.; Wright, D.; Luthey-Schulten, Z. Multiple Alignment of Protein Structures and Sequences for VMD. *Bioinformatics* **2006**, *22*, S04–S06.
- (14) Saphire, E. O.; Parren, P. W.; Pantophlet, R.; Zwick, M. B.; Morris, G. M.; Rudd, P. M.; Dwek, R. A.; Stanfield, R. L.; Burton, D. R.; Wilson, I. A. Crystal Structure of a Neutralizing Human IgG Against HIV-1: a Template for Vaccine Design. *Science* **2001**, *293*, 1155–1159.
- (15) Lipman, N. S.; Jackson, L. R.; Trudel, L. J.; Weis-Garcia, F. Monoclonal Versus Polyclonal Antibodies: Distinguishing Characteristics, Applications, and Information Resources. *ILAR J.* **2005**, *46*, 258–268.
- (16) Keizer, R. J.; Huitema, A. D.; Schellens, J. H.; Beijnen, J. H. Clinical Pharmacokinetics of Therapeutic Monoclonal Antibodies. *Clinical Pharmacokinetics* **2010**, *49*, 493–507.
- (17) Viola, M.; Sequeira, J.; Seiça, R.; Veiga, F.; Serra, J.; Santos, A. C.; Ribeiro, A. J. Subcutaneous Delivery of Monoclonal Antibodies: How Do We Get There? *J. Controlled Release* **2018**, *286*, 301–314.
- (18) Deokar, V.; Sharma, A.; Mody, R.; Volety, S. M. Comparison of Strategies in Development and Manufacturing of Low Viscosity, Ultra-High Concentration Formulation for IgG1 Antibody. *J. Pharm. Sci.* **2020**, *109*, 3579–3589.
- (19) Garidel, P.; Kuhn, A. B.; Schäfer, L. V.; Karow-Zwick, A. R.; Blech, M. High-Concentration Protein Formulations: How High is High? *Eur. J. Pharm. Biopharm.* **2017**, *119*, 353–360.
- (20) Badkar, A.; Gandhi, R.; Davis, S.; LaBarre, M. Subcutaneous Delivery of High-Dose/Volume Biologics: Current Status and Prospect for Future Advancements *Drug Design, Development and Therapy* **2021**, *15*, 159–170.
- (21) Berteau, C.; Filipe-Santos, O.; Wang, T.; Rojas, H. E.; Granger, C.; Schwarzenbach, F. Evaluation of the Impact of Viscosity, Injection Volume, and Injection Flow Rate on Subcutaneous Injection Tolerance. *Medical Devices (Auckland, NZ)* **2015**, *8*, 473.
- (22) Shire, S. J.; Shahrokh, Z.; Liu, J. Challenges in the Development of High Protein Concentration Formulations. *Current trends in Monoclonal Antibody Development and Manufacturing* **2010**, *131*–147.
- (23) Le Basle, Y.; Chennell, P.; Tokhadze, N.; Astier, A.; Sautou, V. Physicochemical Stability of Monoclonal Antibodies: A Review. *J. Pharm. Sci.* **2020**, *109*, 169–190.
- (24) Jiskoot, W.; Hawe, A.; Menzen, T.; Volkin, D. B.; Crommelin, D. J. Ongoing Challenges to Develop High Concentration Monoclonal Antibody-Based Formulations for Subcutaneous Administration: Quo Vadis? *J. Pharm. Sci.* **2022**, *111*, 861–867.
- (25) Kanai, S.; Liu, J.; Patapoff, T. W.; Shire, S. J. Reversible Self-Association of a Concentrated Monoclonal Antibody Solution Mediated by Fab–Fab Interaction that Impacts Solution Viscosity. *J. Pharm. Sci.* **2008**, *97*, 4219–4227.
- (26) Liu, J.; Nguyen, M. D.; Andya, J. D.; Shire, S. J. Reversible Self-Association Increases the Viscosity of a Concentrated Monoclonal Antibody in Aqueous Solution. *J. Pharm. Sci.* **2005**, *94*, 1928–1940.
- (27) Yadav, S.; Liu, J.; Shire, S. J.; Kalonia, D. S. Specific Interactions in High Concentration Antibody Solutions Resulting in High Viscosity. *J. Pharm. Sci.* **2010**, *99*, 1152–1168.
- (28) Binabaji, E.; Ma, J.; Zydny, A. L. Intermolecular Interactions and the Viscosity of Highly Concentrated Monoclonal Antibody Solutions. *Pharm. Res.* **2015**, *32*, 3102–3109.
- (29) Dear, B. J.; Hung, J. J.; Laber, J. R.; Wilks, L. R.; Sharma, A.; Truskett, T. M.; Johnston, K. P. Enhancing Stability and Reducing Viscosity of a Monoclonal Antibody With Cosolutes by Weakening Protein-Protein Interactions. *J. Pharm. Sci.* **2019**, *108*, 2517–2526.
- (30) Esfandiary, R.; Parupudi, A.; Casas-Finet, D.; Gadre, J.; Sathish, H. Mechanism of Reversible Self-Association of a Monoclonal Antibody: Role of Electrostatic and Hydrophobic Interactions. *J. Pharm. Sci.* **2015**, *104* (2), 577–586.
- (31) Tilegenova, C.; Izadi, S.; Yin, J.; Huang, C. S.; Wu, J.; Ellerman, D.; Hymowitz, S. G.; Walters, B.; Salisbury, C.; Carter, P. J. Dissecting the Molecular Basis of High Viscosity of Monospecific and Bispecific IgG Antibodies. *mAbs* **2020**, *12*, 1692764.
- (32) Zeng, Y.; Tran, T.; Wuthrich, P.; Naik, S.; Davagnino, J.; Greene, D. G.; Mahoney, R. P.; Soane, D. S. Caffeine as a Viscosity Reducer for Highly Concentrated Monoclonal Antibody Solutions. *J. Pharm. Sci.* **2021**, *110*, 3594–3604.
- (33) Guo, Z.; Chen, A.; Nassar, R. A.; Helk, B.; Mueller, C.; Tang, Y.; Gupta, K.; Klibanov, A. M. Structure-Activity Relationship for Hydrophobic Salts as Viscosity-Lowering Excipients for Concentrated Solutions of Monoclonal Antibodies. *Pharm. Res.* **2012**, *29*, 3102–3109.
- (34) Srivastava, A.; O'Dell, C.; Bolessa, E.; McLinden, S.; Fortin, L.; Deorkar, N. Viscosity Reduction and Stability Enhancement of Monoclonal Antibody Formulations Using Derivatives of Amino Acids. *J. Pharm. Sci.* **2022**, *111*, 2848–2856.
- (35) Bauer, K. C.; Suhm, S.; Wöll, A. K.; Hubbuch, J. Impact of Additives on the Formation of Protein Aggregates and Viscosity in Concentrated Protein Solutions. *Int. J. Pharm.* **2017**, *516*, 82–90.
- (36) Hong, T.; Iwashita, K.; Shiraki, K. Viscosity Control of Protein Solution by Small Solutes: A Review. *Curr. Protein Pept. Sci.* **2018**, *19* (8), 746–758.
- (37) Proj, M.; Zidar, M.; Lebar, B.; Strašek, N.; Miličić, G.; Žula, A.; Gobec, S. Discovery of Compounds with Viscosity-Reducing Effects on Biopharmaceutical Formulations with Monoclonal Antibodies *Computational and Structural Biotechnology Journal* **2022**, *20*, 5420–5429.
- (38) Li, L.; Kumar, S.; Buck, P. M.; Burns, C.; Lavoie, J.; Singh, S. K.; Warne, N. W.; Nichols, P.; Luksha, N.; Boardman, D. Concentration dependent Viscosity of Monoclonal Antibody Solutions: Explaining Experimental Behavior in terms of Molecular Properties. *Pharm. Res.* **2014**, *31*, 3161–3178.
- (39) Tomar, D. S.; Li, L.; Broulidakis, M. P.; Luksha, N. G.; Burns, C. T.; Singh, S. K.; Kumar, S. In-Silico Prediction of Concentration-Dependent Viscosity Curves for Monoclonal Antibody Solutions. *mAbs* **2017**, *9*, 476–489.
- (40) Apgar, J. R.; Tam, A. S.; Sorm, R.; Moesta, S.; King, A. C.; Yang, H.; Kelleher, K.; Murphy, D.; D'Antona, A. M.; Yan, G.; et al. Modeling and Mitigation of High-Concentration Antibody Viscosity through Structure-Based Computer-Aided Protein Design. *Public Library of Science one* **2020**, *15*, No. e0232713.
- (41) Schmitt, J.; Razvi, A.; Grapentin, C. Predictive Modeling of Concentration-Dependent Viscosity Behavior of Monoclonal Antibody Solutions Using Artificial Neural Networks. *Mabs* **2023**, *15*, 2169440.
- (42) Skar-Gislunge, N.; Camerin, F.; Stradner, A.; Zaccarelli, E.; Schurtenberger, P. Cluster Formation and The Link to Viscosity in Antibody Solutions *arXiv (Soft Condensed Matter)*, 23 Apr 2023, arXiv:2209.05182, ver. 2. DOI: [10.48550/arXiv.2209.05182](https://doi.org/10.48550/arXiv.2209.05182).
- (43) Skar-Gislunge, N.; Camerin, F.; Stradner, A.; Zaccarelli, E.; Schurtenberger, P. Using Cluster Theory to Calculate the Experimental Structure Factors of Antibody Solutions. *Mol. Pharmaceutics* **2023**, *20*, 2738–2753.
- (44) Gentiluomo, L.; Roessner, D.; Streicher, W.; Mahapatra, S.; Harris, P.; Frieß, W. Characterization of Native Reversible Self-Association of a Monoclonal Antibody Mediated by Fab-Fab Interaction. *J. Pharm. Sci.* **2020**, *109*, 443.
- (45) Chowdhury, A.; Manohar, N.; Guruprasad, G.; Chen, A. T.; Lanzaro, A.; Blanco, M.; Johnston, K. P.; Truskett, T. M. Characterizing Experimental Monoclonal Antibody Interactions and Clustering Using a Coarse-Grained Simulation Library and a Viscosity Model. *J. Phys. Chem. B* **2023**, *127*, 1120–1137.
- (46) Sharma, V. K.; Patapoff, T. W.; Kabakoff, B.; Pai, S.; Hilario, E.; Zhang, B.; Li, C.; Borisov, O.; Kelley, R. F.; Chorniy, I.; Zhou, J. Z.; Dill, K. A.; Swartz, T. E. In Silico Selection of Therapeutic Antibodies for Development: Viscosity, Clearance, and Chemical Stability. *Proc. Natl. Acad. Sci. U. S. A.* **2014**, *111*, 18601–18606.
- (47) Lai, P.-K.; Swan, J. W.; Trout, B. L. Calculation of Therapeutic Antibody Viscosity with Coarse-Grained Models, Hydrodynamic

- Calculations and Machine Learning-Based Parameters. *mAbs* **2021**, *13*, 1907882.
- (48) Lai, P.-K.; Gallegos, A.; Mody, N.; Sathish, H. A.; Trout, B. L. Machine Learning Prediction of Antibody aggregation and Viscosity for High Concentration Formulation Development of Protein Therapeutics. *mAbs* **2022**, *14*, 2026208.
- (49) Blanco, M. A. Computational Models for Studying Physical Instabilities in High Concentration Biotherapeutic Formulations. *mAbs* **2022**, *14*, 2044744.
- (50) Forder, J. K.; Ilott, A. J.; Sahin, E.; Roberts, C. J. Simulation of High-Concentration Self-Interactions for Monoclonal Antibodies from Well-Behaved to Poorly-Behaved Systems. *AIChE J.* **2023**, *69*, No. e17965.
- (51) Da Vela, S.; Roosen-Runge, F.; Skoda, M. W.; Jacobs, R. M.; Seydel, T.; Frielinghaus, H.; Sztucki, M.; Schweins, R.; Zhang, F.; Schreiber, F. Effective Interactions and Colloidal Stability of Bovine γ -Globulin in Solution. *J. Phys. Chem. B* **2017**, *121*, 5759–5769.
- (52) Girelli, A.; Rahmann, H.; Begam, N.; Ragulskaya, A.; Reiser, M.; Chandran, S.; Westermeier, F.; Sprung, M.; Zhang, F.; Gutt, C.; Schreiber, F. Microscopic Dynamics of Liquid-Liquid Phase Separation and Domain Coarsening in a Protein Solution Revealed by X-Ray Photon Correlation Spectroscopy. *Phys. Rev. Lett.* **2021**, *126*, 138004.
- (53) Girelli, A.; Beck, C.; Bäuerle, F.; Matsarskaia, O.; Maier, R.; Zhang, F.; Wu, B.; Lang, C.; Czakkel, O.; Seydel, T.; Schreiber, F.; Roosen-Runge, F. Molecular Flexibility of Antibodies Preserved Even in the Dense Phase After Macroscopic Phase Separation. *Mol. Pharmaceutics* **2021**, *18*, 4162–4169.
- (54) Wang, T.; Chen, J.; Du, X.; Feng, G.; Dai, T.; Li, X.; Liu, D. How Neutron Scattering Techniques benefit investigating Structures and Dynamics of Monoclonal Antibody. *Biochimica et Biophysica Acta (BBA) - General Subjects* **2022**, *1866*, 130206.
- (55) Zhang, Z.; Woy, A. M.; Hong, K.; Grapentin, C.; Khan, T. A.; Zarraga, I. E.; Wagner, N. J.; Liu, Y. Adsorption of Non-ionic Surfactant and Monoclonal Antibody on Siliconized Surface Studied by Neutron Reflectometry. *J. Colloid Interface Sci.* **2021**, *584*, 429–438.
- (56) Ruane, S.; Li, Z.; Hollowell, P.; Hughes, A.; Warwicker, J.; Webster, J. R. P.; van der Walle, C. F.; Kalonia, C.; Lu, J. R. Investigating the Orientation of an Interfacially Adsorbed Monoclonal Antibody and Its Fragments Using Neutron Reflection. *Mol. Pharmaceutics* **2023**, *20*, 1643–1656.
- (57) Yearley, E. J.; Godfrin, P. D.; Perevozhikova, T.; Zhang, H.; Falus, P.; Porcar, L.; Nagao, M.; Curtis, J. E.; Gawande, P.; Taing, R.; et al. Observation of Small Cluster Formation in Concentrated Monoclonal Antibody Solutions and Its Implications to Solution Viscosity. *Biophys. J.* **2014**, *106*, 1763–1770.
- (58) Godfrin, P. D.; Zarraga, I. E.; Zarzar, J.; Porcar, L.; Falus, P.; Wagner, N. J.; Liu, Y. Effect of Hierarchical Cluster Formation on The Viscosity of Concentrated Monoclonal Antibody Formulations Studied by Neutron Scattering. *J. Phys. Chem. B* **2016**, *120*, 278–291.
- (59) Grimaldo, M.; Lopez, H.; Beck, C.; Roosen-Runge, F.; Moulin, M.; Devos, J. M.; Laux, V.; Härtlein, M.; Da Vela, S.; Schweins, R.; et al. Protein Short-Time Diffusion in a Naturally Crowded Environment. *J. Phys. Chem. Lett.* **2019**, *10*, 1709–1715.
- (60) Scarcelli, J. J.; Shang, T. Q.; Iskra, T.; Allen, M. J.; Zhang, L. Strategic Deployment of CHO Expression Platforms to Deliver Pfizer's Monoclonal Antibody Portfolio. *Biotechnol. Prog.* **2017**, *33*, 1463–1467.
- (61) Wang, S. S.; Yan, Y. S.; Ho, K. US FDA-Approved Therapeutic Antibodies with High-Concentration Formulation: Summaries and Perspectives. *Antibody Therapeutics* **2021**, *4*, 262–272.
- (62) Frick, B.; Mamontov, E.; van Eijck, L.; Seydel, T. Recent Backscattering Instrument Developments at the ILL and SNS. *Z. Phys. Chem.* **2010**, *224*, 33–60.
- (63) Beck, C.; Girelli, A.; Grapentin, C.; Matsarskaia, O.; Pounot, K.; Schreiber, F.; Seydel, T. Dynamic Cluster Formation, Viscosity, and Diffusion in Monoclonal Antibody Solutions Depending on Antibody Type and Crowding. *ILL Data*, 2021, DOI: [10.5291/ILL-DATA.8-04-908](https://doi.org/10.5291/ILL-DATA.8-04-908).
- (64) Arnold, O.; Bilheux, J.-C.; Borreguero, J.; Buts, A.; Campbell, S. I.; Chapon, L.; Doucet, M.; Draper, N.; Leal, R. F.; Gigg, M.; et al. Mantid - Data Analysis and Visualization Package for Neutron Scattering and μ SR Experiments. *Nucl. Instrum. Methods Phys. Res., Sect. A* **2014**, *764*, 156–166.
- (65) Beck, C.; Pounot, K.; Mosca, I.; Jalarvo, N. H.; Roosen-Runge, F.; Schreiber, F.; Seydel, T. Notes on Fitting and Analysis Frameworks for QENS Spectra of (Soft) Colloid Suspensions. *EPJ. Web Conf.* **2022**, *272*, No. 01004.
- (66) Roosen-Runge, F.; Hennig, M.; Zhang, F.; Jacobs, R. M. J.; Sztucki, M.; Schober, H.; Seydel, T.; Schreiber, F. Protein Self-Diffusion in Crowded Solutions. *Proc. Natl. Acad. Sci. U. S. A.* **2011**, *108*, 11815–11820.
- (67) Grimaldo, M.; Roosen-Runge, F.; Zhang, F.; Seydel, T.; Schreiber, F. Diffusion and Dynamics of γ -Globulin in Crowded Aqueous Solutions. *J. Phys. Chem. B* **2014**, *118*, 7203–7209.
- (68) Grimaldo, M.; Roosen-Runge, F.; Zhang, F.; Schreiber, F.; Seydel, T. Dynamics of Proteins in Solution. *Q. Rev. Biophys.* **2019**, *52*, E7.
- (69) Beck, C.; Grimaldo, M.; Roosen-Runge, F.; Braun, M. K.; Zhang, F.; Schreiber, F.; Seydel, T. Nanosecond Tracer Diffusion as a Probe of The Solution Structure and Molecular Mobility of Protein Assemblies: The Case of Ovalbumin. *J. Phys. Chem. B* **2018**, *122*, 8343–8350.
- (70) Singwi, K.; Sjölander, Å. Diffusive Motions in Water and Cold Neutron Scattering. *Phys. Rev.* **1960**, *119*, 863.
- (71) Fitter, J. Confined Molecular Motions of Globular Proteins Studied in Powder Samples and in Solution. *J. Phys. IV France* **2000**, *10*, No. Pr7-265.
- (72) Bée, M. A Physical Insight into the Elastic Incoherent Structure Factor. *Physica B: Condensed Matter* **1992**, *182*, 323–336.
- (73) Lindner, P.; Schweins, R. The D11 Small-Angle Scattering Instrument: A New Benchmark for SANS. *Neutron News* **2010**, *21*, 15–18.
- (74) Kłosowski, P.; Könnecke, M.; Tischler, J.; Osborn, R. NeXus: A Common Format for the Exchange of Neutron and Synchrotron Data. *Physica B: Condensed Matter* **1997**, *241–243*, 151–153 Proceedings of the International Conference on Neutron Scattering..
- (75) Könnecke, M.; Akeroyd, F. A.; Bernstein, H. J.; Brewster, A. S.; Campbell, S. I.; Clausen, B.; Cottrell, S.; Hoffmann, J. U.; Jemian, P. R.; Männicke, D.; et al. The NeXus Data Format. *J. Appl. Crystallogr.* **2015**, *48*, 301–305.
- (76) Colin, L.; Beck, C.; Buchholz, C.; Grapentin, C.; Matsarskaia, O.; Mosca, I.; Pounot, K.; Reichart, L.; Schreiber, F.; Seydel, T. Tunable Equilibrium Monoclonal Antibody Nanocluster Dispersions at High Concentrations. *ILL Data* 2021. DOI: [10.5291/ILL-DATA.8-04-923](https://doi.org/10.5291/ILL-DATA.8-04-923)
- (77) Acrivos, A. Non-Newtonian Fluids: Rheometry. *Science* **1976**, *191*, 942–942.
- (78) Phillips, J. C.; Braun, R.; Wang, W.; Gumbart, J.; Tajkhorshid, E.; Villa, E.; Chipot, C.; Skeel, R. D.; Kale, L.; Schulten, K. Scalable Molecular Dynamics with NAMD. *J. Comput. Chem.* **2005**, *26*, 1781–1802.
- (79) Huang, J.; MacKerell, A. D., Jr CHARMM36 All-Atom Additive Protein Force Field: Validation Based on Comparison to NMR data. *J. Comput. Chem.* **2013**, *34*, 2135–2145.
- (80) Huang, J.; Rauscher, S.; Nawrocki, G.; Ran, T.; Feig, M.; De Groot, B. L.; Grubmüller, H.; MacKerell, A. D. CHARMM36m: An Improved Force Field for Folded and Intrinsically Disordered Proteins. *Nat. Methods* **2017**, *14*, 71–73.
- (81) Mark, P.; Nilsson, L. Structure and Dynamics of the TIP3P, SPC, and SPC/E Water Models at 298 K. *J. Phys. Chem. A* **2001**, *105*, 9954–9960.
- (82) Martyna, G. J.; Tobias, D. J.; Klein, M. L. Constant Pressure Molecular Dynamics Algorithms. *J. Chem. Phys.* **1994**, *101*, 4177–4189.
- (83) Ryckaert, J.-P.; Ciccotti, G.; Berendsen, H. J. Numerical Integration of the Cartesian Equations of Motion of A System With Constraints: Molecular Dynamics of N-Alkanes. *J. Comput. Phys.* **1977**, *23*, 327–341.
- (84) Grubmüller, H.; Heller, H.; Windemuth, A.; Schulten, K. Generalized Verlet algorithm for Efficient Molecular Dynamics

- Simulations with long-range Interactions. *Mol. Simul.* **1991**, *6*, 121–142.
- (85) Tuckerman, M.; Berne, B. J.; Martyna, G. J. Reversible Multiple Time scale Molecular Dynamics *the. J. Chem. Phys.* **1992**, *97*, 1990–2001.
- (86) Essmann, U.; Perera, L.; Berkowitz, M. L.; Darden, T.; Lee, H.; Pedersen, L. G. A Smooth Particle Mesh Ewald Method. *the Journal of Chemical Physics* **1995**, *103*, 8577–8593.
- (87) Wells, B. A.; Chaffee, A. L. Ewald Summation for Molecular Simulations. *J. Chem. Theory Comput.* **2015**, *11*, 3684–3695.
- (88) Grossfield, A.; Patrone, P. N.; Roe, D. R.; Schultz, A. J.; Siderius, D. W.; Zuckerman, D. M. Best Practices for Quantification of Uncertainty and Sampling Quality in Molecular Simulations [Article v1. 0]. *LiveCoMS* **2019**, *1*, 5067.
- (89) Jurrus, E.; Engel, D.; Star, K.; Monson, K.; Brandi, J.; Felberg, L. E.; Brookes, D. H.; Wilson, L.; Chen, J.; Liles, K.; et al. Improvements to The APBS Biomolecular Solvation Software Suite. *Protein Sci.* **2018**, *27*, 112–128.
- (90) Olsson, M. H.; Søndergaard, C. R.; Rostkowski, M.; Jensen, J. H. PROPKA3: Consistent Treatment of Internal and Surface Residues in Empirical pKa Predictions. *J. Chem. Theory Comput.* **2011**, *7*, 525–537.
- (91) Cock, P. J.; Antao, T.; Chang, J. T.; Chapman, B. A.; Cox, C. J.; Dalke, A.; Friedberg, I.; Hamelryck, T.; Kauff, F.; Wilczynski, B.; et al. BioPython: Freely Available Python Tools for Computational Molecular Biology and Bioinformatics. *Bioinformatics* **2009**, *25*, 1422–1423.
- (92) Abraham, M. J.; Murtola, T.; Schulz, R.; Páll, S.; Smith, J. C.; Hess, B.; Lindahl, E. GROMACS: High Performance Molecular Simulations through Multi-Level Parallelism from Laptops to Supercomputers. *SoftwareX* **2015**, *1–2*, 19–25.
- (93) Páll, S.; Abraham, M. J.; Kutzner, C.; Hess, B.; Lindahl, E. Tackling Exascale Software Challenges in Molecular Dynamics Simulations with GROMACS. In *Solving Software Challenges for Exascale Lecture Notes in Computer Science*; Markidis, S., Laure, E., Eds.; Springer International Publishing: Cham, 2015; pp 3–27.
- (94) Chen, P.-c.; Hub, J. S. Validating Solution Ensembles from Molecular Dynamics Simulation by Wide-Angle X-Ray Scattering Data. *Biophys. J.* **2014**, *107*, 435–447.
- (95) Michaud-Agrawal, N.; Denning, E. J.; Woolf, T. B.; Beckstein, O. MDAnalysis: A Toolkit for the Analysis of Molecular Dynamics Simulations. *J. Comput. Chem.* **2011**, *32*, 2319–2327.
- (96) Gowers, R. J.; Linke, M.; Barnoud, J.; Reddy, T. J. E.; Melo, M. N.; Seyler, S. L.; Domański, J.; Dotson, D. L.; Buchoux, S.; Kenney, I. M.; Beckstein, O. MDAnalysis: A Python Package for the Rapid Analysis of Molecular Dynamics Simulations. *Proc. 15th Python Sci. Conf. (SciPy 2016)*, **2016**, 98–105. .
- (97) Hagberg, A. A.; Schult, D. A.; Swart, P. J. Exploring Network, Dynamics, and Function Using NetworkX. *Proc. 7th Python in Sci. Conf. (SciPy 2008)*, **2008**, 11–15.
- (98) Tokuyama, M.; Oppenheim, I. On The Theory of Concentrated Hard-Sphere Suspensions. *Physica A: Statistical Mechanics and its Applications* **1995**, *216*, 85–119.
- (99) Banchio, A. J.; Nägele, G. Short-Time Transport Properties in Dense Suspensions: from Neutral to Charge-Stabilized Colloidal Spheres *the. J. Chem. Phys.* **2008**, *128*, 104903.
- (100) Roosen-Runge, F.; Schurtenberger, P.; Stradner, A. Self-Diffusion of Nonspherical Particles Fundamentally Conflicts With Effective Sphere Models. *J. Phys.: Condens. Matter* **2021**, *33*, 154002.
- (101) Ortega, A.; Amorós, D.; García de La Torre, J. Prediction of Hydrodynamic and other Solution Properties of rigid Proteins from Atomic-and Residue-Level Models. *Biophys. J.* **2011**, *101*, 892–898.
- (102) Harris, L. J.; Larson, S. B.; Hasel, K. W.; McPherson, A. Refined Structure of an Intact IgG2a Monoclonal Antibody. *Biochemistry* **1997**, *36*, 1581–1597.
- (103) Cho, C. H.; Urquidi, J.; Singh, S.; Robinson, G. W. Thermal Offset Viscosities of Liquid H₂O, D₂O, and T₂O. *J. Phys. Chem. B* **1999**, *103*, 1991–1994.
- (104) Bonner, A.; Furtado, P. B.; Almogren, A.; Kerr, M. A.; Perkins, S. J. Implications of the Near-Planar Solution Structure of Human Myeloma Dimeric IgA1 for Mucosal Immunity and IgA Nephropathy. *J. Immunol.* **2008**, *180*, 1008–1018.
- (105) Pedregosa, F.; Varoquaux, G.; Gramfort, A.; Michel, V.; Thirion, B.; Grisel, O.; Blondel, M.; Prettenhofer, P.; Weiss, R.; Dubourg, V.; et al. Scikit-learn: Machine Learning in Python. *J. Mach. Learn. Res.* **2011**, *12*, 2825–2830.
- (106) Pedersen, J. S. Analysis of Small-Angle Scattering Data from Colloids and Polymer Solutions: Modeling and Least-Squares Fitting. *Adv. Colloid Interface Sci.* **1997**, *70*, 171–210.
- (107) Lindner, P.; Zemb, T. *Neutrons, X-rays, and Light: Scattering Methods Applied to Soft Condensed Matter*; Elsevier: North-Holland, 2002.
- (108) Debye, P. Zerstreuung von Röntgenstrahlen. *Ann. Phys.* **1915**, *351*, 809–823.
- (109) Hansen, J.-P.; McDonald, I. R. *Theory of Simple Liquids*, 3rd ed.; Academic Press: Amsterdam, 2006.
- (110) Feigin, L. A.; Svergun, D. I. *Structure Analysis by Small-Angle X-ray and Neutron Scattering*; Plenum Press: New York, 1987.
- (111) Guinier, A.; Fournet, G. *Small-Angle Scattering of X-rays*; Wiley: New York, 1955; Vol. 14.
- (112) Svergun, D. I.; Koch, M. H. J. Small-Angle Scattering Studies of Biological Macromolecules in Solution *Rep. Prog. Phys.* **2003**, *66*, 1735–1782.
- (113) Gunton, J.; Shirayev, A.; Pagan, D. *Protein Condensation: Kinetic Pathways to Crystallization and Disease*; Cambridge University Press, 2007.
- (114) Schärtl, W. *Light Scattering from Polymer Solutions and Nanoparticle Dispersions*; Springer, 2007.
- (115) Noro, M. G.; Frenkel, D. Extended Corresponding-States Behavior for Particles With Variable Range Attractions. *J. Chem. Phys.* **2000**, *113*, 2941–2944.
- (116) Bonneté, F.; Vivarès, D. Interest of the Normalized Second Virial Coefficient and Interaction Potentials for Crystallizing Large Macromolecules. *Acta Crystallographica D* **2002**, *58*, 1571–1575.
- (117) Kline, S. R. Reduction and Analysis of SANS and USANS Data Using IGOR Pro. *J. Appl. Crystallogr.* **2006**, *39*, 895–900.
- (118) Yearley, E. J.; Zarraga, I. E.; Shire, S. J.; Scherer, T. M.; Gokarn, Y.; Wagner, N. J.; Liu, Y. Small-Angle Neutron Scattering Characterization of Monoclonal Antibody Conformations and Interactions at High Concentrations. *Biophys. J.* **2013**, *105*, 720–731.
- (119) Castellanos, M. M.; Pathak, J. A.; Leach, W.; Bishop, S. M.; Colby, R. H. Explaining the Non-Newtonian Character of Aggregating Monoclonal Antibody Solutions Using Small-Angle Neutron Scattering. *Biophys. J.* **2014**, *107*, 469–476.
- (120) Lilyestrom, W. G.; Yadav, S.; Shire, S. J.; Scherer, T. M. Monoclonal Antibody Self-Association, Cluster Formation, and Rheology at High Concentrations. *J. Phys. Chem. B* **2013**, *117*, 6373–6384.
- (121) von Bülow, S.; Siggel, M.; Linke, M.; Hummer, G. Dynamic cluster Formation Determines Viscosity and Diffusion in Dense Protein Solutions. *Proc. Natl. Acad. Sci. U. S. A.* **2019**, *116*, 9843–9852.